CCFE
CULHAM CENTRE FOR FUSION ENERGY

UK Atomic Energy Authority

UKAEA-CCFE-PR(23)100

K D Lawson, E Pawelec, I H Coffey, M Groth, A G Meigs

Observation of low temperature VUV tungsten emission in JET divertor plasmas

Observation of low temperature VUV tungsten emission in JET divertor plasmas

K D Lawson, E Pawelec, I H Coffey, M Groth, A G Meigs

This is a preprint of a paper submitted for publication in Physica Scripta

Observation of low temperature VUV tungsten emission in JET divertor plasmas

K D Lawson[1], E Pawelec[2], I H Coffey[1,3], M Groth[4], E Litherland-Smith[1], A G Meigs[1], S Scully[1] & JET Contributors*

EUROfusion Consortium, JET, Culham Science Centre, Abingdon, OX14 3DB, UK

[1]UKAEA/CCFE, Culham Science Centre, Abingdon, OX14 3DB, UK

[2]Institute of Physics, Opole University, Oleska 48, 45-052 Opole, Poland

[3]Astrophysics Research Centre, School of Mathematics and Physics, Queen's University Belfast, Belfast, BT7 1NN, Northern Ireland, UK

[4]Aalto University, Otakaari 1, Espoo, 02150, Finland

Abstract

The properties of tungsten make it ideal for use as a plasma facing surface in the divertor of large plasma machines such as JET and ITER. However, the intense heat and particle fluxes that fall on the divertor surfaces lead to its release from these surfaces into the plasma and it is necessary to model its transport from the divertor and plasma edge into the plasma core. This requires measurement of spectral features over a wide temperature range. In large machines the W influx is often determined from W I line intensities, there being few measurements of discrete W lines from other low ionization stages. Their observation is highly desirable because the transport of neutral W differs markedly from that of the W ions. A change in the line of sight of a VUV survey spectrometer on JET to view directly into the divertor has led to the observation of numerous discrete low temperature W lines in the VUV spectral region. The spectrum of an intense influx in which W IV to W VIII features are observed has been analysed in order to provide spectral classifications so that these lines can be used for diagnostic purposes. The first observation of a VUV low temperature W magnetic dipole (M1) transition is reported for the W VIII ionization stage. The analysis shows where further line identifications are needed and that the provision of the highest quality atomic data for these ionization stages is desirable. Lines from W VI and W VII are used to illustrate their use in determining the electron temperature of the emitting plasma region and the W concentration. Dependences of the W line intensities on plasma parameters shows the optimal conditions for the W release and suggests the site of its release.

1. Introduction

Present-day, large plasma machines employ a cold, dense plasma, contained in a divertor, to control and limit the heat and particle fluxes that reach the machine's plasma-facing surfaces (Loarte *et al.*, 2007). Nevertheless, the surfaces within the divertor must still be able to withstand high heat loads. Although C is widely used as a wall material in many present-day machines, its use in a reactor is not possible due to its retention of hydrogenic species. This would lead to unacceptably high inventories of T in the reactor. An alternative element for the plasma-facing surfaces in a divertor is W, which has a high tensile strength, high melting point and low vapour pressure (Matthews *et al.*, 2007). A disadvantage of W is its high atomic number, Z, which means that there is significant radiation and consequently cooling of

the plasma when the W ions reach the plasma core. It is therefore essential to understand the mechanisms for the release and transport of W into the core, either from the divertor plates or from the walls of the machine onto which W has been deposited during previous plasma operations (e.g. Dux *et al.*, 2011, Yang *et al.*, 2020). JET, with its ITER-like wall (ILW) of Be in the main chamber and W in the divertor, is ideally suited to such studies (Casson *et al.*, 2020).

The spectroscopy of highly ionized W is becoming better understood, both the passive emission and that due to charge exchange to W ions from neutral beam heating (Thorman *et al*, 2021). This enables analyses of the W transport within the core plasma (Angioni *et al.,* 2014, 2016, Valisa *et al.,* 2016). However, precise measurements of the W source are still problematic. On JET the most frequently used W influx measurement is that of neutral W, in particular the visible 4008.75 Å line. However, the transport of neutrals and ions is very different and so it is important to have, in addition, measurements of low temperature W ions. Near UV W II lines have been observed in JET (van Rooij *et al*., 2013), although are not seen routinely. Other visible W lines from the W II to W V ionization stages are also observed, although only during extreme events such as the W melting experiment (Coenen *et al*., 2015). With increasing temperatures, the emission from W occurs at higher energies and is seen further into the UV spectral region. Most of the emission from low W ionization stages is seen as broad, overlapping transition arrays in the VUV spectral region (Pawelec *et al*., 2017). However, there are a number of observations of discrete lines from ions such as W IV to W XIV made both by the injection of W into low temperature plasma machines, for example the SSPX spheromak (Clementson *et al*., 2010), the LHD stellarator (Oishi *et al*., 2016) and the HL-2A tokamak (Dong *et al*., 2019), and the use of W in other plasma sources such as EBIT devices (Clementson *et al*., 2015, Mita *et al*., 2017) and vacuum sparks (Ryabtsev *et al*., 2015). In the larger plasma machines, it was expected that the low W ionization stages, to which these discrete lines belong, will have a limited spatial extent, since there is a wide range of ionization stages within the machine's temperature range. Together with the low W concentration, this will make their observation difficult, particularly along lines-of-sight through the narrow plasma edge with its steep gradients. However, this is less true when viewing the divertor plasma, where a larger emission region is possible. A VUV spectrometer that had previously observed the divertor throat during the JET-ILW campaigns has been realigned to observe the divertor plasma and this has led to discrete lines from low ionization stages of W being identified in JET plasmas. The different lines-of-sight of the VUV spectrometer are illustrated in figure 1. The most intense of these lines had been observed previously, although the complexity of the spectrum in this wavelength region meant that they had not been identified as belonging to low ionization stages of W. Figure 2 shows a comparison of the time histories of one of the most intense of the low temperature W lines, the W VII, 261.39 Å line, in a pair of similar hybrid pulses (numbers 90271 and 96362), whose plasma parameters are illustrated in figure 3. It can be seen that realigning the spectrometer view led to a significantly higher intensity of the W VII line.

Section 2 describes the VUV instruments used to record the W spectrum and section 3 presents the spectral analysis. The W features are most obvious as a result of occasional influxes and are particularly evident during ELMy H-mode pulses. The plasma parameters necessary for their observation during such pulses are discussed in section 4. An analysis of these parameters indicates the plasma facing surfaces from which the W is usually released. The W VI and W VII spectra allow the electron temperature of the emitting region to be determined and illustrative calculations are given in section 5. The available atomic data does not indicate a density sensitivity at densities of ~10^{19}-10^{20} m^{-3}, although at the highest densities encountered in divertor plasmas, ~10^{21} m^{-3}, some sensitivity is possible. This section also describes their use in determining W concentrations. The conclusions form section 6.

2. Experimental arrangement

The diagnostic used to record the XUV/VUV divertor spectrum on JET, known locally as KT7, consists of three separate spectrometers (Wolf *et al*., 1995), a double SPRED spectrometer (Fonck *et al*. 1982) and a Schwob-Fraenkel instrument (Schwob *et al*., 1987). All have the same line-of-sight viewing from the top of the machine towards the divertor, as illustrated in figure 1. The diagnostic can be tilted poloidally allowing the line-of-sight to view anywhere from the inner divertor to the Scrap-Off Layer (SOL) above the throat of the outer divertor. During the JET-ILW campaigns, the view has been fixed looking towards the throat above the outer divertor, this giving a line-of-sight passing through the plasma centre in many of the magnetic configurations used in JET so as to allow a routine and consistent measurement of the W concentration. The W spectral features seen with the Schwob-Fraenkel spectrometer at wavelengths of 42-54 Å was used for this measurement. The advantages of viewing the divertor plasma for a more detailed analysis of its behaviour was considered before the C38 campaign (May 2018-December 2019) and the diagnostic realigned so that the line-of-sight was centred on the outer horizontal divertor plate (tile 5). With this view the spectrometer observes emission directly from the divertor, but still with the line-of-sight passing close to the plasma centre so as not to compromise the measurement of the W concentration.

The spectra analysed were recorded with the double SPRED spectrometers. The spectrometers are enclosed in stainless steel shielding to reduce noise due to both neutrons and γ-rays, with 15 cm of shielding between the plasma and detectors and 5 cm thickness at the back and sides. The detectors are microchannel plate (MCP) / phosphor combinations which are coupled to a Reticon photodiode array via a fibre optic bundle. It is the interaction of the neutrons and γ-rays with the MCP, with its high gain, that is of most concern. A shielding of 15cm of steel was expected to reduce the 2.5 MeV neutron flux by a factor of ~8 and that of the 8 MeV γ-rays by a factor of ~17. Comparisons were made shortly after the double SPRED instrument was commissioned with the JET VUV SPRED survey spectrometer, which has a horizontal line-of-sight and is unshielded. These suggested that the background due to nuclear reaction products was a factor of ~7 lower in the double SPRED instruments than in the unshielded

spectrometer. The MCPs have a CuI coating in order to enhance the electron emission. The detector integration time can be varied down to a minimum of 11 ms, the readout time of the detectors, with 15-25 ms being used routinely.

Both spectrometers have toroidal holographic gratings, with, respectively, ruling densities of 450 (KT7/1) and 2105 g.mm^{-1} (KT7/2). They have extended and shifted spectral ranges compared with the standard SPREDs, the former observing 148-1480 Å with a spectral resolution of ~5 Å, the latter 140-444 Å with a spectral resolution of ~1 Å. Usually the gratings supplied with the SPREDs enhance the first and third spectral orders. In the case of the longer wavelength spectrometer (KT7/1), the second spectral order is found to be more intense than the third. Due to the combination of the wavelength coverage and the fall in sensitivity at the shortest wavelengths, higher spectral orders are less important for the short wavelength instrument.

The detectors have 2048 pixels, although a detector fault in the short wavelength detector in which adjacent pairs of pixels output the same intensity, effectively halved the useful number of pixels for this detector. In both detectors the signal from alternate pixels is processed by different amplifiers. A small mismatch in their gains for the long wavelength detector made it necessary to smooth the spectrum by averaging the intensities of adjacent pixels.

A simple and reliable spectral line integration method is employed, in which a fixed number of pixels on either side of the line centre define an integration range and the background to be subtracted (Lawson *et al*., 1987). This method takes advantage of the similarity of the spectral line profile throughout the wavelength range of the spectrometers and overcomes the difficulty of treating the unusual line profile in which intense lines develop extreme line wings (Lawson and Peacock, 1988). When a line is unblended the integration is performed by Simpson's rule, a ±5 pixel range being used for the long wavelength detector and a ±3 pixel range for the short wavelength detector with its halved number of useful pixels. These ranges cover the most intense part of the line profiles. In cases of blended lines a simple fitting procedure is used in which the centre of the line is taken to be Gaussian in shape. The integration is then performed by Simpson's rule over the appropriate number of pixels using the fitted profiles in order to ensure the integrity of the absolute sensitivity calibration. The procedure for obtaining sensitivity calibrations of the spectrometers involves an *in situ* method in which a relative calibration is derived first and then is fixed on an absolute scale by the use of branching ratios with calibrated visible spectrometers. Cross-calibrations with other VUV instruments ensure a consistent set of calibrations for the suite of XUV and VUV spectrometers on JET. The method is described by Lawson *et al.* (2021).

3. Spectral analysis

The occasional influx provides the most intense spectra and therefore those most suited to spectral analysis. A particularly strong influx occurred in an ELMy H-mode pulse 95012 at 14.34 s. The VUV spectrum for this pulse is shown in figures 4 to 12. The W emission reached a peak at 14.37 s and then

rapidly decayed in ~15 ms. This pulse is ideal in having very few contaminating lines from other impurities, which can be a significant problem in this spectral region. Some weak C, O and metal lines are observed, but can easily be accounted for in the analysis by comparing the pre-influx spectrum at 14.32 s with that being analysed. As is always found the analysis is limited by the spectral resolution of the spectrometers being used. This is a particular consideration given the complexity of the low temperature W spectrum, but nevertheless the results are thought valuable in showing which W ionization stages are observed in a large tokamak, which lines might be useful for diagnostic purposes and where further line identifications and other atomic data are needed. The analysis demonstrates that unless a spectrometer with a high spectral resolution is available for diagnostic measurements the choice of diagnostic lines must account for blending from all possible ionization stages. It also highlights that the available atomic data in the form of Photon Emission Coefficients (PECs) does not necessarily match the spectral lines observed; this is the case for many elements, not just W.

The main analysis uses the comprehensive list of identifications given in the NIST database (Kramida *et al*. 2020), which provides accurate wavelengths and the intensities of previous observations. It must be recognized that the relative intensities of emission features within an ionization stage can vary between different plasma sources. However, being able to match the many features observed in the JET spectrum with the most intense of the listed lines suggests that it is a valid approach to use these intensities as a guide to which lines are expected in large plasma machines. Some differences are found; for example, the well resolved spectrum recorded by Oishi *et al.* (2016) on LHD shows the W VII line at 533.63 Å to be more intense than that at 530.95 Å which is consistent with the NIST listing, whereas the opposite appears to be the case in the JET spectrum with the 530.95 Å line weakly observed, while the 533.63 Å line, if present, forming part of the background. Nevertheless, no gross discrepancies were found in the analysis of the JET spectrum. The analysed spectra were recorded with the double SPRED instruments viewing the machine's divertor and lines from ionization stages of W IV to W VIII have been identified. Table 1 lists the W lines identified in the spectrum recorded with the short wavelength high resolution grating and table 2 that with the lower resolution longer wavelength detector, with annotated spectra shown in figures 4 to 8 and 9 to 12, respectively. The mixing of states in these ionization stages can be extreme and hence the only way to uniquely define a level is to give its energy. Consequently, the energies of both upper and lower levels of each transition are listed in addition to their spectroscopic classifications. As an example, there are a number of W VIII lines whose upper configurations are $4f^{12}5p^{6}5d_{5/2}$ and $4f^{12}5p^{6}5d_{7/2}$. Inspection of the energies shows that there are, in fact, respectively, 9 and 5 different levels identified with these configurations. The leading contributing states to these levels are given in table 3. More information about all the states involved and their percentage contributions to the level are given in the NIST energy level database or the original papers presenting the identifications. In many cases the spectral features consist of a blend of more than one line making the precise composition of the feature uncertain. In these cases, the intensity of the previous observations of a line

is used to judge which transitions are most likely to form the observed feature. A number of lines are observed for which no identification in the published literature has been found and these lines are listed in tables 4 and 5 for the short and long wavelength detectors, respectively. They are labelled in figures 4 to 12 by a green 'W'. The accuracy of the wavelengths of the unblended lines listed in these tables is ±0.2 and ±1.0 Å, respectively. There are four spectral regions where the lines are so dense (essentially unresolved transition arrays) that the spectrum is plotted separately with an expanded wavelength scale. These are figures 4b (197-203 Å), 7b (322-341 Å), 9b (440-525 Å) and 11b (960-1017 Å); the shape of the envelope of the spectrum depends as much on the density of lines as their intensities. For example, in the wavelength range 440 - 525 Å there are 44 W V lines listed in the NIST database, 25 of which have an intensity ≥30 and 102 W VII lines, 36 with an intensity ≥ 100.

3.1. W VIII magnetic dipole transition

Of particular interest is the observation of the W VIII magnetic dipole (M1) transition at 1137.1±0.5 Å. This is predicted in the NIST database (Kramida *et al*., 2020) at a wavelength of 1137.79 Å and is thought to be the first observation in the VUV spectral region of an M1 transition in a low ionization stage of W. Ratios between M1 and allowed (E1) transitions are expected to be density sensitive, which gives the possibility of measuring the electron density of the plasma region from which the W VIII line is emitted. However, the necessary atomic data is not available for this transition at present. This observation is particularly valuable in that the line is reasonably well isolated from intense neighbours, falling between two weak W IV lines at 1135.15 and 1140.27Å. The former most likely gives rise to the asymmetric line profile seen in the JET spectrum.

3.2. Short wavelength high resolution spectrum

The identifications made in the short wavelength spectrum of JET pulse 95012 are listed in Table 1 and it can be seen that the majority of W features can be identified with transitions listed in the NIST database. Nevertheless, there are a significant number of lines which are unidentified (table 4). Clementson *et al*., (2015) present spectra recorded with the Livermore electron beam ion trap facility, EBIT-I, which allows the ionization stage to be determined for some of these lines, although no definite identification has been possible. For these, the ionization stage is indicated in table 4. A comparison of the JET spectrum with those of Clementson *et al*. suggest that unidentified W VIII transitions at 194.65 and 207.99 Å will form part of the blends of lines at 194.40/194.53 Å and 208.42/208.54 Å, respectively, which are seen in the JET spectrum. Further, the unidentified W VI lines at 221.45 and 222.05 Å will be blended with the W VIII lines at 221.44 and 221.92 Å, respectively. In an analysis of a spectrum from the Livermore SSPX spheromak, Clementson *et al*. (2010) suggest that the line at 210.2 Å, which is also seen in the JET spectrum, is a possible candidate for a W VI transition. However, this is not confirmed by their later EBIT-I spectra, so no ionization stage can be given for this line at present.

A comparison of the EBIT-I spectra of Clementson *et al*. at energies of 43 and 57 eV in their figure 1 shows that the behaviour of the line at 313.58 Å is closer to that of other W VI lines (a reduction of the intensity of the 313.58 Å line relative to other W VI lines of ~30%) rather than the W VII lines (~50-60% reduction). This raises the possibility that this line is a blend of a lower ionization stage transition together with the W VII transition with which it is usually identified. The presence of a significant lower temperature component to the line would explain the discrepancy found in trying to match the W VII line intensities measured in the JET spectrum with theory (see section 5).

3.3. Long wavelength low resolution spectrum

At wavelengths above 495 Å comparisons were made with the spectrum of Oishi *et al*. (2016) recorded on LHD. This includes lines from the ionization stages W III to W VII. The comparisons proved to be of particular value given the much higher spectral resolution of the LHD spectrum than that of the JET long wavelength spectrum. Nevertheless, more lines were observed in the JET spectrum, particularly at longer wavelengths even allowing for the absence of the W VIII features in the LHD spectrum. For example, W IV lines at 908.22 and 910.06 Å can be seen clearly in the JET spectrum, as can the W V line at 1125.31 Å, but are very weak or absent from the LHD spectrum. Oishi *et al.* identify a line at 497 Å with the W VII line at 497.38 Å. An identification of this line with the 497.24 Å, W VII line would seem more likely given the larger J values for the latter transition. This would be consistent with the line intensities given by Sugar and Kaufman (1975) and is the identification preferred in the present work. Oishi *et al.* include the 1051.50 Å W IV line as part of a blend with O III and O IV lines. However, this line is very weak and thought unlikely to contribute. Of greater intensity is the 1050.93 Å line which can be seen as a shoulder to a N III line in their spectrum. It is this line that is expected to contribute to the long wavelength shoulder of the second order W VII line at 1046.50 Å. It is noted that both the wavelength and intensity of the line at 1160 Å suggests that the unidentified W line at 1159.5 Å is the most significant component of the blend, the 1161.36 and 1161.37 Å W IV lines falling to longer wavelengths than that of the line peak and expected to be comparatively weak. Oishi *et al.* do not observe W VIII and, at longer wavelengths, they observe few W VII lines. This would suggest that any intense unidentified W line at longer wavelengths (table 5) that is not observed by Oishi *et al*. belongs to one of these ionization stages.

3.4. Non-W components to the observed lines

Lines due to elements other than W that make a significant contribution to the observed lines are indicated in both the figures and tables. In addition, there are a few lines which have small components due to non-W lines. The most notable are the weak O V and metal lines on the short wavelength side of the 165.41Å Ni XXVI line and unidentified lines at 732.4 and 937.00 Å, respectively, contributing to the 731.73/733.56 Å W V and 935.77 Å W V / 935.86 Å W IV blends. These contributions are small and are not large enough to account for the intensities observed in the analysed spectrum.

3.5. Use of discrete low temperature W lines for diagnostic purposes

One use of this analysis is to inform proposals for diagnostic measurements using VUV low temperature W features. This is demonstrated by deriving estimates of the electron temperature of the plasma region from which W VI and W VII features are emitted as well as the concentration of these ions. These are presented in section 5. However, to illustrate the importance of understanding the details of the spectrum when making such measurements an example involving W IV lines is given. Ballance *et al*. (2013) present high quality data for the electron impact excitation and ionization for this ionization stage and propose four lines at 1099.05, 1119.71, 1172.47 and 1186.17 Å, illustrated in their figure 9, for W influx measurements. A comparison with the JET spectrum shown in figure 11a shows that a significantly higher spectral resolution than that of the JET instrument would be required once W lines from other ionization stages and possible other impurity contaminants to the spectrum are taken into account. If the second spectral order is present then a spectral resolution of ~0.5 Å would be required to ensure that the four lines can be observed unblended. This is higher than would normally be available for most survey spectrometers on large plasma machines, being similar to that of the instrument used on LHD by Oishi *et al*. (2016). In the absence of the second order spectrum the constraint is relaxed somewhat, but would still need to be better than ~2.5 Å.

3.6. W lines belonging to higher ionization stages

The spectrum of pulse 95012 includes features from the ionization stages W IV to W VIII. Higher ionization stages, particularly at wavelengths shorter than ~194 Å, are observed in other JET pulses. These spectra are extremely complex and although there are some published spectra for this wavelength range, such as the EBIT spectra of Clementson *et al*. (2015) and Mita *et al*. (2017), the only known identifications are those of Ryabtsev *et al.* (2015) for W IX. The JET observations for these higher ionization stages will be discussed in a future publication.

Table 1. Identifications of W lines observed with the short wavelength high resolution detector

Wavelength (Å)	Ionization stage	Intensity	Energy levels (cm^{-1})	Lower level	Upper level	References	Comments
150.20	W VII	~6.9e+4	0 - 665763	$4f^{14}5p^6\ ^1S_0$	$4f^{13}(^2F_{5/2})5p^6 6d\ (5/2,3/2)\ 1$	1	sh 149.91 Cr XXI
150.28	W VII	~6.9e+4	0 - 665445	$4f^{14}5p^6\ ^1S_0$	$4f^{13}(^2F_{5/2})5p^6 6d\ (5/2,5/2)\ 1$	1	sh 150.20
151.89	W VII	~1.3e+5	0 - 658367	$4f^{14}5p^6\ ^1S_0$	$4f^{14}5p^5(^2P_{3/2})6d\ (3/2,5/2)\ 1$	1	bl 151.5 O V
153.85	W VII	~7.8e+4	0 - 649982	$4f^{14}5p^6\ ^1S_0$	$4f^{13}(^2F_{7/2})5p^6 6d\ (7/2,5/2)\ 1$	1	bl 153.51 Cu XXVII
161.26	W VIII	8.0e+4	1233 - 621343	$4f^{14}5p^5\ ^2P_{3/2}$	$4f^{13}5p^5(5/2,1/2)_2 6s\ (2,1/2)\ 5/2$	2,3	sh 164.3
163.59	W VIII	~1.1e+5	0 - 611283	$4f^{13}5p^6\ ^2F_{7/2}$	$4f^{13}5p^5(5/2,1/2)_3 6s\ (3,1/2)\ 7/2$	2,3	
165.37	W VIII	~3.0e+5	17410 - 622123	$4f^{13}5p^6\ ^2F_{5/2}$	$4f^{13}5p^5(5/2,1/2)_2 6s\ (2,1/2)\ 3/2$	2,3	bl 165.41 Ni XXVI
166.83	W VIII	7.5e+4	0 - 599423	$4f^{13}5p^6\ ^2F_{7/2}$	$4f^{13}5p^5(7/2,1/2)_4 6s\ (4,1/2)\ 9/2$	2,3	
167.38	W VIII	8.5e+4	0 - 597436	$4f^{13}5p^6\ ^2F_{7/2}$	$4f^{13}5p^5(7/2,1/2)_3 6s\ (3,1/2)\ 5/2$	2,3	

168.39	W VIII	1.1e+5	17410 - 611283	$4f^{13}5p^6\ ^2F_{5/2}$	$4f^{13}5p^5(5/2,1/2)_3 6s\ (3,1/2)\ 7/2$	2,3	
168.98	W VIII	7.6e+4	17410 - 609206	$4f^{13}5p^6\ ^2F_{5/2}$	$4f^{13}5p^5(5/2,1/2)_3 6s\ (3,1/2)\ 5/2$	2,3	
172.29	W VIII	6.2e+4	1233 - 581635	$4f^{14}5p^5\ ^2P_{3/2}$	$4f^{14}5p^4(^1D_2)6s\ (2,1/2)\ 5/2$	2,3	
175.20	W VIII	1.1e+5	1233 - 572004	$4f^{14}5p^5\ ^2P_{3/2}$	$4f^{14}5p^4(^3P_1)6s\ (1,1/2)\ 1/2$	2,3	
188.16	W VII	4.3e+5	0 - 531465	$4f^{14}5p^6\ ^1S_0$	$4f^{14}5p^5(^2P_{1/2})6s\ (1/2,1/2)\ 1$	1	
189.62	W VIII	~7.3e+4	0 - 527376	$4f^{13}5p^6\ ^2F_{7/2}$	$4f^{13}5p^5(5/2,3/2)_4 6s\ (4,1/2)\ 7/2$	2,3	bl 189.67
189.67	W VIII	~7.3e+4	1233 - 528462	$4f^{14}5p^5\ ^2P_{3/2}$	$4f^{14}5p^4(^1D_2)5d\ (2,5/2)\ 1/2$	2,3	bl 189.62
193.61	W VIII	~3.2e+5	0 - 516493	$4f^{13}5p^6\ ^2F_{7/2}$	$4f^{13}5p^5 5d\ 5/2$	2,3	bl 194.04 Ni XVI
194.40	W VIII	~2.0e+5	0 - 514413	$4f^{13}5p^6\ ^2F_{7/2}$	$4f^{13}5p^5(5/2,3/2)_3 6s\ (3,1/2)\ 7/2$	2,3	bl 194.04 Ni XVI, 194.53
194.53	W VIII	~2.4e+5	0 - 514063	$4f^{13}5p^6\ ^2F_{7/2}$	$4f^{13}5p^5(7/2,3/2)_2 6s\ (2,1/2)\ 5/2$	2,3	bl 194.40, 194.65
195.60	W VIII	~1.5e+5	17410 - 528652	$4f^{13}5p^6\ ^2F_{5/2}$	$4f^{13}5p^5(5/2,3/2)_1 6s\ (1,1/2)\ 3/2$	2,3	bl 196.09
196.09	W VIII	~1.1e+5	17410 - 527376	$4f^{13}5p^6\ ^2F_{5/2}$	$4f^{13}5p^5(5/2,3/2)_4 6s\ (4,1/2)\ 7/2$	2,3	bl 195.60
197.84	W VIII	~5.0e+5	17410 - 522881	$4f^{13}5p^6\ ^2F_{5/2}$	$4f^{12}5p^6 5d\ 3/2$	2,3	bl 197.94
197.94	W VIII	~5.0e+5	17410 - 522610	$4f^{13}5p^6\ ^2F_{5/2}$	$4f^{12}(^1S_0)5p^6 5d\ (0,5/2)\ 5/2$	2,3	bl 197.84, 198.17
198.17	W VIII	~6.8e+5	0 - 504615	$4f^{13}5p^6\ ^2F_{7/2}$	$4f^{13}5p^5(7/2,3/2)_5 6s\ (5,1/2)\ 9/2$	2,3	bl 197.94, 198.23
198.23	W VIII	~6.8e+5	17410 - 521876	$4f^{13}5p^6\ ^2F_{5/2}$	$4f^{13}5p^5(5/2,3/2)_2 6s\ (2,1/2)\ 5/2$	2,3	bl 198.17, 198.78
198.78	W VIII	~8.0e+5	0 - 503071	$4f^{13}5p^6\ ^2F_{7/2}$	$4f^{13}5p^5(7/2,3/2)_4 6s\ (4,1/2)\ 7/2$	2,3	bl 198.23
199.88	W VIII	~7.8e+5	0 - 500313	$4f^{13}5p^6\ ^2F_{7/2}$	$4f^{13}5p^5(7/2,3/2)_3 6s\ (3,1/2)\ 5/2$	2,3	bl 200.37
200.37	W VIII	~9.2e+5	17410 - 516493	$4f^{13}5p^6\ ^2F_{5/2}$	$4f^{13}5p^5 5d\ 5/2$	2,3	bl 199.88, 200.48
200.48	W VIII	~9.2e+5	0 - 498792	$4f^{13}5p^6\ ^2F_{7/2}$	$4f^{13}5p^5(7/2,1/2)_4 5d\ (4,3/2)\ 7/2$	2,3	bl 200.37, 200.79
200.79	W VIII	~8.5e+5	0 - 498037	$4f^{13}5p^6\ ^2F_{7/2}$	$4f^{13}5p^5(7/2,1/2)_4 5d\ (4,3/2)\ 5/2$	2,3	bl 200.48, 201.08
201.08	W VIII	~9.8e+5	1233 - 498541	$4f^{14}5p^5\ ^2P_{3/2}$	$4f^{14}5p^4 5d\ 3/2$	2,3	bl 200.79, 201.12
201.12	W VIII	~9.8e+5	17410 - 514628	$4f^{13}5p^6\ ^2F_{5/2}$	$4f^{13}5p^5(5/2,3/2)_3 6s\ (3,1/2)\ 5/2$	2,3	bl 201.08, 201.21
201.21	W VIII	~1.1e+6	17410 - 514413	$4f^{13}5p^6\ ^2F_{5/2}$	$4f^{13}5p^5(5/2,3/2)_3 6s\ (3,1/2)\ 7/2$	2,3	bl 201.12, 201.29
201.29	W VIII	~1.1e+6	1233 - 498037	$4f^{14}5p^5\ ^2P_{3/2}$	$4f^{13}5p^5(7/2,1/2)_4 5d\ (4,3/2)\ 7/2$	2,3	bl 201.21, 201.74
201.74	W VIII	~1.4e+6	0 - 495690	$4f^{13}5p^6\ ^2F_{7/2}$	$4f^{13}5p^5(7/2,1/2)_3 5d\ (3,3/2)\ 9/2$	2,3	bl 201.29, 201.87
201.87	W VIII	~1.4e+6	17410 - 512790	$4f^{13}5p^6\ ^2F_{5/2}$	$4f^{13}5p^5(5/2,1/2)_2 5d\ (2,3/2)\ 7/2$	2,3	bl 201.74
202.25	W VIII	~3.7e+5	89123 - 583560	$4f^{14}5p^5\ ^2P_{1/2}$	$4f^{14}5p^4(^1D_2)6s\ (2,1/2)\ 3/2$	2,3	sh 201.87
203.62	W VIII	~1.1e+5	1233 - 492337	$4f^{14}5p^5\ ^2P_{3/2}$	$4f^{14}5p^4(^1D_2)5d\ (2,3\ /2)1/2$	2,3	sh 202.25
205.22	W VIII	~5.1e+5	17410 - 504691	$4f^{13}5p^6\ ^2F_{5/2}$	$4f^{12}5p^6 5d\ 3/2$	2,3	bl 205.48
205.48	W VIII	~5.1e+5	1233 - 487901	$4f^{14}5p^5\ ^2P_{3/2}$	$4f^{14}5p^4(^3P_2)6s\ (2,1/2)\ 3/2$	2,3	bl 205.22
207.47	W VIII	~2.5e+5	1233 - 483243	$4f^{14}5p^5\ ^2P_{3/2}$	$4f^{13}5p^5(5/2,1/2)_2 5d\ (2,5/2)\ 3/2$	2,3	sh 208.42
208.42	W VIII	~5.3e+5	1233 - 481035	$4f^{14}5p^5\ ^2P_{3/2}$	$4f^{14}5p^4 5d\ 5/2$	2,3	bl 207.99
208.54	W VIII	~3.5e+5	89123 - 568644	$4f^{14}5p^5\ ^2P_{1/2}$	$4f^{14}5p^4(^3P_1)6s\ (1,1/2)\ 3/2$	2,3	sh 208.42
211.02	W VIII	2.1e+5	1233 - 475117	$4f^{14}5p^5\ ^2P_{3/2}$	$4f^{14}5p^4 5d\ 3/2$	2,3	
214.22	W VIII	2.6e+5	1233 - 468034	$4f^{14}5p^5\ ^2P_{3/2}$	$4f^{12}5p^6 5d\ 5/2$	2,3	
215.06	W VIII	~2.9e+5	1233 - 466219	$4f^{14}5p^5\ ^2P_{3/2}$	$4f^{12}5p^6 5d\ 5/2$	2,3	sh 216.22
216.22	W VII	3.7e+6	0 - 462496	$4f^{14}5p^6\ ^1S_0$	$4f^{14}5p^5(^2P_{1/2})5d\ (1/2,3/2)\ 1$	1	
216.59	W VIII	~2.4e+6	1233 - 462927	$4f^{14}5p^5\ ^2P_{3/2}$	$4f^{13}5p^5(5/2,1/2)_2 5d\ (2,3/2)\ 3/2$	2,3	sh 216.22
218.43	W VIII	~3.8e+5	0 - 457815	$4f^{13}5p^6\ ^2F_{7/2}$	$4f^{12}(^1I_6)5p^6 5d\ (6,5/2)\ 9/2$	2,3	bl 218.51
218.51	W VIII	~3.8e+5	0 - 457652	$4f^{13}5p^6\ ^2F_{7/2}$	$4f^{13}5p^5(7/2,1/2)_4 5d\ (4,5/2)\ 5/2$	2,3	bl 218.43
221.44	W VIII	~1.6e+5	1233 - 452821	$4f^{14}5p^5\ ^2P_{3/2}$	$4f^{12}5p^6 5d\ 3/2$	2,3	bl 221.45, sh 221.92
221.92	W VIII	~2.6e+5	17410 - 468034	$4f^{13}5p^6\ ^2F_{5/2}$	$4f^{12}5p^6 5d\ 5/2$	2,3	bl 222.05, sh 222.88

223.84	W VII	1.3e+6	0 - 446749	$4f^{14}5p^6\ {}^1S_0$	$4f^{14}5p^5(^2P_{3/2})6s$ (3/2,1/2) 1	1	
227.62	W VIII	3.8e+5	89123 - 528462	$4f^{14}5p^5\ {}^2P_{1/2}$	$4f^{14}5p^4(^1D_2)5d$ (2,5/2) 1/2	2,3	
229.01	W VIII	~1.4e+5	17410 - 454067	$4f^{13}5p^6\ {}^2F_{5/2}$	$4f^{12}(^1I_6)5p^65d$ (6,5/2) 7/2	2,3	bl 229.54
229.54	W VIII	~1.5e+5	0 - 435658	$4f^{13}5p^6\ {}^2F_{7/2}$	$4f^{14}5p^4(^1D_2)5d$ (2,3/2) 7/2	2,3	bl 229.01
231.63	W VIII	~9.8e+4	1233 - 432963	$4f^{14}5p^5\ {}^2P_{3/2}$	$4f^{12}5p^65d$ 5/2	2,3	bl 232.18
232.18	W VIII	~2.2e+5	0 - 430708	$4f^{13}5p^6\ {}^2F_{7/2}$	$4f^{12}5p^65d$ 7/2	2,3	bl 231.63, 232.29
232.29	W VIII	~2.2e+5	17410 - 447909	$4f^{13}5p^6\ {}^2F_{5/2}$	$4f^{12}5p^65d$ 5/2	2,3	bl 232.18
233.22	W VIII	~3.1e+5	0 - 428777	$4f^{13}5p^6\ {}^2F_{7/2}$	$4f^{12}5p^65d$ 7/2	2,3	bl 233.71
233.71	W VIII	~3.7e+5	17410 - 445286	$4f^{13}5p^6\ {}^2F_{5/2}$	$4f^{12}5p^65d$ 5/2	2,3	bl 233.22, 234.15 Ni XXVI
239.09	W VIII	~4.7e+5	17410 - 435658	$4f^{13}5p^6\ {}^2F_{5/2}$	$4f^{14}5p^4(^1D_2)5d$ (2,3/2) 7/2	2,3	bl 238.6
240.11	W VIII	~2.1e+5	0 - 416481	$4f^{13}5p^6\ {}^2F_{7/2}$	$4f^{12}5p^65d$ 9/2	2,3	sh 239.09
241.87	W VIII	~2.3e+5	0 - 413450	$4f^{13}5p^6\ {}^2F_{7/2}$	$4f^{12}5p^65d$ 9/2	2,3	bl 242.82
242.82	W VIII	~1.8e+5	0 - 411832	$4f^{13}5p^6\ {}^2F_{7/2}$	$4f^{12}5p^65d$ 7/2	2,3	bl 241.87
245.05	W VIII	~1.2e+5	0 - 408086	$4f^{13}5p^6\ {}^2F_{7/2}$	$4f^{12}5p^65d$ 7/2	2,3	bl 245.48
245.48	W VIII	~1.2e+5	17410 - 424781	$4f^{13}5p^6\ {}^2F_{5/2}$	$4f^{12}5p^65d$ 5/2	2,3	bl 245.05
246.36	W VIII	2.0e+5	0 - 405907	$4f^{13}5p^6\ {}^2F_{7/2}$	$4f^{12}(^3H_5)5p^65d$ (5,3/2) 9/2	2,3	
248.51	W VIII	~5.3e+5	17410 - 419811	$4f^{13}5p^6\ {}^2F_{5/2}$	$4f^{12}(^3H_5)5p^65d$ (5,5/2) 5/2	2,3	bl 248.65
248.65	W VIII	~7.4e+5	17410 - 419585	$4f^{13}5p^6\ {}^2F_{5/2}$	$4f^{12}(^3H_5)5p^65d$ (5,5/2) 7/2	2,3	bl 248.51, 248.77
248.77	W VIII	~7.4e+5	0 - 401984	$4f^{13}5p^6\ {}^2F_{7/2}$	$4f^{14}5p^45d$ 5/2	2,3	bl 248.65, 249.19 Ni XVII
249.53	W VIII	~5.0e+5	1233 - 401984	$4f^{14}5p^5\ {}^2P_{3/2}$	$4f^{14}5p^45d$ 5/2	2,3	bl 249.19 Ni XVII, 249.87
249.87	W VIII	~2.9e+5	0 - 400203	$4f^{13}5p^6\ {}^2F_{7/2}$	$4f^{12}(^3F_4)5p^65d$ (4,3/2) 9/2	2,3	bl 249.53
250.98	W VIII	~2.4e+5	17410 - 415852	$4f^{13}5p^6\ {}^2F_{5/2}$	$4f^{12}5p^65d$ 5/2	2,3	bl 251.59
251.59	W VIII	~2.2e+5	17410 - 414888	$4f^{13}5p^6\ {}^2F_{5/2}$	$4f^{12}(^3F_3)5p^65d$ (3,3/2) 7/2	2,3	bl 250.98, 252.20
252.20	W VIII	~2.4e+5	0 - 396505	$4f^{13}5p^6\ {}^2F_{7/2}$	$4f^{13}5p^55d$ 7/2	2,3	bl 251.59, 252.74
252.74	W VIII	~4.1e+5	1233 - 396894	$4f^{14}5p^5\ {}^2P_{3/2}$	$4f^{13}5p^55d$ 3/2	2,3	bl 252.20, 252.86
252.86	W VIII	~4.1e+5	0 - 395471	$4f^{13}5p^6\ {}^2F_{7/2}$	$4f^{13}5p^55d$ 7/2	2,3	bl 252.74, 253.54
253.54	W VIII	~4.3e+5	17410 - 411832	$4f^{13}5p^6\ {}^2F_{5/2}$	$4f^{12}5p^65d$ 7/2	2,3	bl 252.86, 253.54
253.54	W VIII	~4.3e+5	17410 - 411819	$4f^{13}5p^6\ {}^2F_{5/2}$	$4f^{12}5p^65d$ 5/2	2,3	bl 253.54, 253.65
253.65	W VIII	~5.0e+5	1233 - 395474	$4f^{14}5p^5\ {}^2P_{3/2}$	$4f^{14}5p^45d$ 1/2	2,3	bl 253.54, 253.81
253.81	W VIII	~5.5e+5	0 - 393992	$4f^{13}5p^6\ {}^2F_{7/2}$	$4f^{12}5p^65d$ 7/2	2,3	bl 253.65, 254.30
254.30	W VIII	~6.3e+5	17410 - 410654	$4f^{13}5p^6\ {}^2F_{5/2}$	$4f^{12}5p^65d$ 7/2	2,3	bl 253.81, 254.55
254.55	W VIII	~6.8e+5	17410 - 410258	$4f^{13}5p^6\ {}^2F_{5/2}$	$4f^{13}5p^5(5/2,3/2)_45d$ (4,5/2) 3/2	2,3	bl 254.30, 254.93
254.93	W VIII	~3.3e+5	17410 - 409676	$4f^{13}5p^6\ {}^2F_{5/2}$	$4f^{12}5p^65d$ 5/2	2,3	bl 254.55
255.40	W VIII	2.2e+5	0 - 391541	$4f^{13}5p^6\ {}^2F_{7/2}$	$4f^{13}5p^55d$ 9/2	2,3	
258.60	W VIII	2.4e+5	0 - 386704	$4f^{13}5p^6\ {}^2F_{7/2}$	$4f^{13}5p^55d$ 5/2	2,3	
259.42	W VIII	2.9e+5	1233 - 386704	$4f^{14}5p^5\ {}^2P_{3/2}$	$4f^{13}5p^55d$ 5/2	2,3	
261.39	W VII	~3.8e+6	0 - 382577	$4f^{14}5p^6\ {}^1S_0$	$4f^{14}5p^5(^2P_{3/2})5d$ (3/2,5/2) 1	1	bl 261.77
261.77	W VIII	~1.7e+6	0 - 382019	$4f^{13}5p^6\ {}^2F_{7/2}$	$4f^{13}5p^5(7/2,3/2)_25d$ (2,5/2) 7/2	2,3	bl 261.39, 261.85
261.85	W VIII	~1.4e+6	1233 - 383133	$4f^{14}5p^5\ {}^2P_{3/2}$	$4f^{13}5p^5(7/2,3/2)_25d$ (2,5/2) 5/2	2,3	bl 261.77
262.54	W VIII	~3.7e+5	0 - 380899	$4f^{13}5p^6\ {}^2F_{7/2}$	$4f^{13}5p^55d$ 9/2	2,3	sh 261.85
263.79	W VIII	6.4e+4	17410 - 396505	$4f^{13}5p^6\ {}^2F_{5/2}$	$4f^{13}5p^55d$ 7/2	2,3	
264.64	W VIII	~2.1e+5	0 - 377867	$4f^{13}5p^6\ {}^2F_{7/2}$	$4f^{13}5p^55d$ 5/2	2,3	bl 264.64
264.64	W VIII	~2.1e+5	17410 - 395276	$4f^{13}5p^6\ {}^2F_{5/2}$	$4f^{13}5p^5(5/2,3/2)_15d$ (1,5/2) 5/2	2,3	bl 264.64

265.17	W VIII	1.9e+5	0 - 377119	$4f^{13}5p^6\ ^2F_{7/2}$	$4f^{13}5p^5 5d\ 9/2$	2,3	
265.92	W VIII	1.9e+5	1233 - 377288	$4f^{14}5p^5\ ^2P_{3/2}$	$4f^{13}5p^5(7/2,3/2)_2 5d\ (2,5/2)\ 3/2$	2,3	
267.52	W VIII	~7.4e+4	89123 - 462927	$4f^{14}5p^5\ ^2P_{1/2}$	$4f^{13}5p^5(5/2,1/2)_2 5d\ (2,3/2)\ 3/2$	2,3	sh 267.8
289.53	W VII	1.0e+6	0 - 345394	$4f^{14}5p^6\ ^1S_0$	$4f^{13}(^2F_{5/2})5p^6 5d\ (5/2,5/2)\ 1$	1	
294.37	W VII	1.7e+6	0 - 339705	$4f^{14}5p^6\ ^1S_0$	$4f^{13}(^2F_{5/2})5p^6 5d\ (5/2,3/2)\ 1$	1	
302.28	W VII	1.6e+6	0 - 330825	$4f^{14}5p^6\ ^1S_0$	$4f^{13}(^2F_{7/2})5p^6 5d\ (7/2,5/2)\ 1$	1	
313.58	W VII	1.1e+6	0 - 318899	$4f^{14}5p^6\ ^1S_0$	$4f^{14}5p^5(^2P_{3/2})5d\ (3/2,3/2)\ 1$	1	bl W VI T
324.51	W VII	~3.1e+5	335411 - 643569	$4f^{13}(^2F_{5/2})5p^6 5d\ (5/2,3/2)\ 4$	$4f^{13}(^2F_{5/2})5p^6 5f\ (5/2,5/2)\ 5$	4	bl 324.56
324.56	W VII	~3.1e+5	318185 - 626291	$4f^{13}(^2F_{7/2})5p^6 5d\ (7/2,3/2)\ 5$	$4f^{13}(^2F_{7/2})5p^6 5f\ (7/2,5/2)\ 6$	4	bl 324.51
325.36	W VII	9.9e+4	320693 - 628049	$4f^{13}(^2F_{7/2})5p^6 5d\ (7/2,3/2)\ 3$	$4f^{13}(^2F_{7/2})5p^6 5f\ (7/2,5/2)\ 4$	4	
326.41	W VII	~2.1e+5	320693 - 627053	$4f^{13}(^2F_{7/2})5p^6 5d\ (7/2,3/2)\ 3$	$4f^{13}(^2F_{7/2})5p^6 5f\ (7/2,5/2)\ 3$	4	bl 326.64
326.64	W VII	~2.1e+5	322527 - 628672	$4f^{13}(^2F_{7/2})5p^6 5d\ (7/2,3/2)\ 4$	$4f^{13}(^2F_{7/2})5p^6 5f\ (7/2,5/2)\ 5$	4	bl 326.41, 326.65
326.65	W VII	~2.1e+5	340530 - 646673	$4f^{14}5p^5(^2P_{3/2})5d\ (3/2,5/2)\ 4$	$4f^{13}(^2F_{5/2})5p^6 5f\ (5/2,7/2)\ 3$	4	bl 326.64
327.31	W VII	1.7e+5	322527 - 628049	$4f^{13}(^2F_{7/2})5p^6 5d\ (7/2,3/2)\ 4$	$4f^{13}(^2F_{7/2})5p^6 5f\ (7/2,5/2)\ 4$	4	
329.34	W VII	~1.5e+5	343093 - 646733	$4f^{13}(^2F_{5/2})5p^6 5d\ (5/2,3/2)\ 3$	$4f^{13}(^2F_{5/2})5p^6 5f\ (5/2,5/2)\ 4$	4	bl 329.77
329.77	W VII	~2.0e+5	327044 - 630282	$4f^{13}(^2F_{7/2})5p^6 5d\ (7/2,5/2)\ 6$	$4f^{13}(^2F_{7/2})5p^6 5f\ (7/2,7/2)\ 6$	4	bl 329.34
330.28	W VII	~1.3e+5	339705 - 642481	$4f^{13}(^2F_{5/2})5p^6 5d\ (5/2,3/2)\ 1$	$4f^{13}(^2F_{5/2})5p^6 5f\ (5/2,5/2)\ 1$	4	bl 330.28
330.28	W VII	~1.3e+5	343093 - 645867	$4f^{13}(^2F_{5/2})5p^6 5d\ (5/2,3/2)\ 3$	$4f^{13}(^2F_{5/2})5p^6 5f\ (5/2,5/2)\ 3$	4	bl 330.28
331.19	W VII	8.3e+4	328020 - 629962	$4f^{13}(^2F_{7/2})5p^6 5d\ (7/2,5/2)\ 2$	$4f^{13}(^2F_{7/2})5p^6 5f\ (7/2,7/2)\ 2$	4	
332.14	W VII	~7.2e+4	328020 - 629102	$4f^{13}(^2F_{7/2})5p^6 5d\ (7/2,5/2)\ 2$	$4f^{13}(^2F_{7/2})5p^6 5f\ (7/2,7/2)\ 3$	4	sh 332.84
332.84	W VII	~1.4e+5	329950 - 630395	$4f^{13}(^2F_{7/2})5p^6 5d\ (7/2,5/2)\ 4$	$4f^{13}(^2F_{7/2})5p^6 5f\ (7/2,7/2)\ 5$	4	bl 332.84
332.84	W VII	~1.4e+5	327044 - 627487	$4f^{13}(^2F_{7/2})5p^6 5d\ (7/2,5/2)\ 6$	$4f^{13}(^2F_{7/2})5p^6 5f\ (7/2,7/2)\ 7$	4	bl 332.84, 333.3
334.31	W VII	~1.3e+5	346385 - 645507	$4f^{13}(^2F_{5/2})5p^6 5d\ (5/2,5/2)\ 5$	$4f^{13}(^2F_{5/2})5p^6 5f\ (5/2,7/2)\ 6$	4	bl 334.9
336.44	W VII	~5.5e+4	335172 - 632406	$4f^{14}5p^5(^2P_{3/2})5d\ (3/2,3/2)\ 3$	J = 2	4	sh 337.05
337.05	W VII	9.7e+4	333095 - 629791	$4f^{13}(^2F_{7/2})5p^6 5d\ (7/2,5/2)\ 3$	$4f^{13}(^2F_{7/2})5p^6 5f\ (7/2,7/2)\ 4$	4	
337.86	W VII	~4.9e+4	351600 - 647578	$4f^{13}(^2F_{5/2})5p^6 5d\ (5/2,5/2)\ 3$	$4f^{13}(^2F_{5/2})5p^6 5f\ (5/2,7/2)\ 4$	4	sh 338.54
338.54	W VII	~2.1e+5	352478- 647862	$4f^{13}(^2F_{5/2})5p^6 5d\ (5/2,5/2)\ 4$	$4f^{13}(^2F_{5/2})5p^6 5f\ (5/2,7/2)\ 5$	4	bl 338.55
338.55	W VII	~2.1e+5	335017 - 630395	$4f^{13}(^2F_{7/2})5p^6 5d\ (7/2,5/2)\ 5$	$4f^{13}(^2F_{7/2})5p^6 5f\ (7/2,7/2)\ 5$	4	bl 338.54, 338.68
338.68	W VII	~2.1e+5	335017 - 630282	$4f^{13}(^2F_{7/2})5p^6 5d\ (7/2,5/2)\ 5$	$4f^{13}(^2F_{7/2})5p^6 5f\ (7/2,7/2)\ 6$	4	bl 338.55
340.19	W VII	2.8e+4	333095 - 627053	$4f^{13}(^2F_{7/2})5p^6 5d\ (7/2,5/2)\ 3$	$4f^{13}(^2F_{7/2})5p^6 5f\ (7/2,5/2)\ 3$	4	
345.38	W VII	~3.4e+4	343305 - 632838	$4f^{14}5p^5(^2P_{3/2})5d\ (3/2,5/2)\ 2$	J=2	4	bl 345.71
345.71	W VII	~4.1e+4	340530 - 629791	$4f^{14}5p^5(^2P_{3/2})5d\ (3/2,5/2)\ 4$	$4f^{13}(^2F_{7/2})5p^6 5f\ (7/2,7/2)\ 4$	4	bl 345.38
382.15	W VI	1.1e+6	0 - 261681	$5d\ ^2D_{3/2}$	$5f\ ^2F_{5/2}$	5	
394.13	W VI	1.4e+6	8709 - 262430	$5d\ ^2D_{5/2}$	$5f\ ^2F_{7/2}$	5	
395.30	W VI	~1.2e+5	8709 - 261681	$5d\ ^2D_{5/2}$	$5f\ ^2F_{5/2}$	5	sh 394.13
399.29	W V	3.5e+4	6245 - 256688	$5d^2\ ^3F_3$	$5d(^2D_{3/2})7p\ (3/2,3/2)\ 2$	6	
405.88	W V	1.3e+4	11519 - 257895	$5d^2\ ^3F_4$	$5d(^2D_{3/2})7p\ (3/2,3/2)\ 3$	6	
410.33	W V	~4.0e+5	16331 - 260035	$5d^2\ ^3P_1$	$5d(^2D_{5/2})7p\ (5/2,1/2)\ 2$	6	bl 410.42
410.42	W V	~4.0e+5	22615 - 266271	$5d^2\ ^3P_2$	$5d(^2D_{5/2})7p\ (5/2,3/2)\ 2$	6	bl 410.33, 410.87
410.87	W V	~5.8e+5	22346 - 265733	$5d^2\ ^1G_4$	$5d(^2D_{5/2})7p\ (5/2,3/2)\ 3$	6	bl 410.42, 411.32
411.32	W V	~5.9e+5	22615 - 265733	$5d^2\ ^3P_2$	$5d(^2D_{5/2})7p\ (5/2,3/2)\ 3$	6	bl 410.87, 411.61
411.61	W V	~4.7e+5	13742 - 256688	$5d^2\ ^1D_2$	$5d(^2D_{3/2})7p\ (3/2,3/2)\ 2$	6	bl 411.32, 411.91
411.91	W V	~3.7e+4	16331 - 259100	$5d^2\ ^3P_1$	$5d(^2D_{3/2})7p\ (3/2,3/2)\ 0$	6	bl 411.61, 412.05 Cr XIV

412.46	W V	~2.3e+4	16331 - 258778	$5d^2\ ^3P_1$	$5d(^2D_{3/2})7p$ (3/2,3/2) 1	6	bl 412.05 Cr XIV
423.77	W V	~2.1e+4	12839 - 248815	$5d^2\ ^3P_0$	$5d(^2D_{5/2})5f$ (5/2,7/2) 1	6	sh 424.7
428.80	W V	3.6e+4	6245 - 239456	$5d^2\ ^3F_3$	$5d(^2D_{5/2})5f$ (5/2,5/2) 3	7	
430.65	W V	~1.5e+5	0 - 232210	$5d^2\ ^3F_2$	$5d(^2D_{3/2})5f$ (3/2,5/2) 3	7	bl 431.05
431.05	W V	~1.5e+5	6245 - 238239	$5d^2\ ^3F_3$	$5d(^2D_{5/2})5f$ (5/2,5/2) 4	7	bl 430.65
435.02	W V	7.8e+4	0 - 229873	$5d^2\ ^3F_2$	$5d(^2D_{3/2})5f$ (3/2,7/2) 3	7	
436.01	W V	4.6e+4	6245 - 235598	$5d^2\ ^3F_3$	$5d(^2D_{5/2})5f$ (5/2,7/2) 4	7	
437.25	W V	5.6e+4	0 - 228702	$5d^2\ ^3F_2$	$5d(^2D_{3/2})5f$ (3/2,5/2) 2	7	
438.42	W V	1.8e+5	11519 - 239614	$5d^2\ ^3F_4$	$5d(^2D_{5/2})5f$ (5/2,7/2) 5	7	
439.99	W V	~1.7e+4	16331 - 243609	$5d^2\ ^3P_1$	$5d(^2D_{5/2})5f$ (5/2,5/2) 1	7	sh 441.07
441.07	W V	3.4e+4	11519 - 238239	$5d^2\ ^3F_4$	$5d(^2D_{5/2})5f$ (5/2,5/2) 4	7	

bl - blend sh - line on shoulder
References: - 1 – Sugar and Kaufman, 1975 2 – Ryabtsev *et al*., 2013 3 – Deprince & Quinet, 2015
4 – Wyart et al., 1981 5 – Sugar and Kaufman, 1979 6 – Churilov *et al*., 1996 7 – Kildiyarova *et al*., 1996

Table 2. Identifications of W lines observed with the long wavelength lower resolution detector

Wavelength (Å)	Ionization stage	Intensity	Energy levels (cm^{-1})	Lower level	Upper level	References	Comments
442.55	W V	~4.1e+4	6245 - 232210	$5d^2\ ^3F_3$	$5d(^2D_{3/2})5f$ (3/2,5/2) 3	7	sh 443.04
443.04	W V	~4.7e+4	13742 - 239456	$5d^2\ ^1D_2$	$5d(^2D_{5/2})5f$ (5/2,5/2) 3	7	sh 444.85
444.85	W V	~8.2e+4	22346 - 247139	$5d^2\ ^1G_4$	$5d(^2D_{5/2})5f$ (5/2,5/2) 5	7	bl 446.27
446.27	W V	~9.2e+4	11519 - 235598	$5d^2\ ^3F_4$	$5d(^2D_{5/2})5f$ (5/2,7/2) 4	7	bl 444.85, 447.17
447.17	W V	~8.9e+4	6245 - 229873	$5d^2\ ^3F_3$	$5d(^2D_{3/2})5f$ (3/2,7/2) 3	7	bl 446.27, 447.98
447.98	W V	~9.0e+4	12839 - 236062	$5d^2\ ^3P_0$	$5d(^2D_{3/2})5f$ (3/2,5/2) 1	7	bl 447.17, 448.51
448.51	W V	~8.6e+4	6245 - 229205	$5d^2\ ^3F_3$	$5d(^2D_{3/2})5f$ (3/2,7/2) 4	7	bl 447.98
449.65	W V	~5.7e+4	16331 - 238727	$5d^2\ ^3P_1$	$5d(^2D_{5/2})5f$ (5/2,5/2) 2	7	sh 448.51
451.89	W V	~1.0e+4	6245 - 227536	$5d^2\ ^3F_3$	$5d(^2D_{3/2})5f$ (3/2,5/2) 4	7	sh 449.65
453.85	W V	~2.7e+4	22615 - 242953	$5d^2\ ^3P_2$	$5d(^2D_{5/2})5f$ (5/2,7/2) 2	7	bl 454.42
454.42	W V	~3.9e+4	13742 - 233804	$5d^2\ ^1D_2$	$5d(^2D_{3/2})5f$ (3/2,7/2) 2	7	bl 453.85, 454.50
454.50	W V	~3.9e+4	22615 - 242636	$5d^2\ ^3P_2$	$5d(^2D_{5/2})5f$ (5/2,7/2) 3	7	bl 454.42, 455.42
455.42	W V	~4.8e+4	11519 - 231099	$5d^2\ ^3F_4$	$5d(^2D_{3/2})5f$ (3/2,7/2) 5	7	bl 454.50
457.73	W V	~1.0e+4	13742 - 232210	$5d^2\ ^1D_2$	$5d(^2D_{3/2})5f$ (3/2,5/2) 3	7	sh 455.42
459.83	W V	~1.5e+4	16331 - 233804	$5d^2\ ^3P_1$	$5d(^2D_{3/2})5f$ (3/2,7/2) 2	7	bl 460 C III
462.68	W V	~3.3e+4	13742 - 229873	$5d^2\ ^1D_2$	$5d(^2D_{3/2})5f$ (3/2,7/2) 3	7	bl 462.93
462.93	W V	~3.6e+4	11519 - 227536	$5d^2\ ^3F_4$	$5d(^2D_{3/2})5f$ (3/2,5/2) 4	7	bl 462.68, 464 O II
468.93	W V	~3.5e+4	22346 - 235598	$5d^2\ ^1G_4$	$5d(^2D_{5/2})5f$ (5/2,7/2) 4	7	bl 468.30 Ni XXVI
479.04	W V	3.6e+4	22346 - 231099	$5d^2\ ^1G_4$	$5d(^2D_{3/2})5f$ (3/2,7/2) 5	7	
483.91	W VII	~8.4e+4	327044 - 533693	$4f^{13}(^2F_{7/2})5p^65d$ (7/2,5/2) 6	$4f^{13}(^2F_{7/2})5p^66p$ (7/2,3/2) 5	1	bl 484.48
484.48	W VII	~9.9e+4	328020 - 534428	$4f^{13}(^2F_{7/2})5p^65d$ (7/2,5/2) 2	$4f^{13}(^2F_{7/2})5p^66p$ (7/2,3/2) 2	1	bl 483.91, 487.09
487.09	W VII	~9.8e+4	346385 - 551684	$4f^{13}(^2F_{5/2})5p^65d$ (5/2,5/2) 5	$4f^{13}(^2F_{5/2})5p^66p$ (5/2,3/2) 4	1	bl 484.48, 487.35
487.35	W V	~9.6e+4	22346 - 227536	$5d^2\ ^1G_4$	$5d(^2D_{3/2})5f$ (3/2,5/2) 4	7	bl 487.09, 488.07
488.07	W VII	~8.9e+4	329950 - 534838	$4f^{13}(^2F_{7/2})5p^65d$ (7/2,5/2) 4	$4f^{13}(^2F_{7/2})5p^66p$ (7/2,3/2) 3	1	bl 487.35

496.42	W VII	~1.5e+5	311441 - 512882	$4f^{13}(^2F_{7/2})5p^6 5d$ (7/2,3/2) 2	$4f^{13}(^2F_{7/2})5p^6 6p$ (7/2,1/2) 3	1	bl 496.52
496.52	W VII	~1.6e+5	335017 - 536420	$4f^{13}(^2F_{7/2})5p^6 5d$ (7/2,5/2) 5	$4f^{13}(^2F_{7/2})5p^6 6p$ (7/2,3/2) 4	1	bl 496.42, 497.24
497.24	W VII	~1.9e+5	352478 - 553588	$4f^{13}(^2F_{5/2})5p^6 5d$ (5/2,5/2) 4	$4f^{13}(^2F_{5/2})5p^6 6p$ (5/2,3/2) 3	1	bl 496.52, 498.38 Ni XVII
500.84	W VII	~6.8e+4	335172 - 534838	$4f^{14}5p^5(^2P_{3/2})5d$ (3/2,3/2) 3	$4f^{13}(^2F_{7/2})5p^6 6p$ (7/2,3/2) 3	1	sh 498.38 Ni XVII
503.33	W VII	~8.8e+4	335017 - 533693	$4f^{13}(^2F_{7/2})5p^6 5d$ (7/2,5/2) 5	$4f^{13}(^2F_{7/2})5p^6 6p$ (7/2,3/2) 5	1	bl 503.53
503.53	W VII	~9.0e+4	340530 - 539127	$4f^{14}5p^5(^2P_{3/2})5d$ (3/2,5/2) 4	$4f^{14}5p^5(^2P_{3/2})6p$ (3/2,3/2) 3	1	bl 503.33
511.63	W VII	~1.4e+5	318185 - 513640	$4f^{13}(^2F_{7/2})5p^6 5d$ (7/2,3/2) 5	$4f^{13}(^2F_{7/2})5p^6 6p$ (7/2,1/2) 4	1	bl 512.62
512.62	W VII	~1.4e+5	335411 - 530489	$4f^{13}(^2F_{5/2})5p^6 5d$ (5/2,3/2) 4	$4f^{13}(^2F_{5/2})5p^6 6p$ (5/2,1/2) 3	1	bl 511.63, 512.63 He II
518.28	W VII	~6.8e+4	320693 - 513640	$4f^{13}(^2F_{7/2})5p^6 5d$ (7/2,3/2) 3	$4f^{13}(^2F_{7/2})5p^6 6p$ (7/2,1/2) 4	1	sh 520.32
520.32	W VII	~9.8e+4	320693 - 512882	$4f^{13}(^2F_{7/2})5p^6 5d$ (7/2,3/2) 3	$4f^{13}(^2F_{7/2})5p^6 6p$ (7/2,1/2) 3	1	sh 522.77
523.25	W VII	~2.5e+5	322527 - 513640	$4f^{13}(^2F_{7/2})5p^6 5d$ (7/2,3/2) 4	$4f^{13}(^2F_{7/2})5p^6 6p$ (7/2,1/2) 4	1	bl 522.77
525.34	W VII	~1.1e+5	322527 - 512882	$4f^{13}(^2F_{7/2})5p^6 5d$ (7/2,3/2) 4	$4f^{13}(^2F_{7/2})5p^6 6p$ (7/2,1/2) 3	1	sh 523.25
527.62	W VII	~4.6e+4	354111 - 543641	$4f^{14}5p^5(^2P_{3/2})5d$ (3/2,5/2) 3	$4f^{14}5p^5(^2P_{3/2})6p$ (3/2,3/2) 2	1	sh 525.34
530.95	W VII	2.9e+4	343093 - 531434	$4f^{13}(^2F_{5/2})5p^6 5d$ (5/2,3/2) 3	$4f^{13}(^2F_{5/2})5p^6 6p$ (5/2,1/2) 2	1	
536.92	W VII	~4.1e+4	330825 - 517074	$4f^{13}(^2F_{7/2})5p^6 5d$ (7/2,5/2) 1	$4f^{14}5p^5(^2P_{3/2})6p$ (3/2,1/2) 1	1	bl 537.35
537.35	W VII	~4.1e+4	333095 - 519194	$4f^{13}(^2F_{7/2})5p^6 5d$ (7/2,5/2) 3	$4f^{14}5p^5(^2P_{3/2})6p$ (3/2,1/2) 2	1	bl 536.92, 538 C III
542.95	W VII	~1.4e+4	335017 - 519194	$4f^{14}5p^5(^2P_{3/2})5d$ (3/2,3/2) 2	$4f^{14}5p^5(^2P_{3/2})6p$ (3/2,1/2) 2	1	bl 543.41
543.41	W VII	~1.7e+4	335172 - 519194	$4f^{14}5p^5(^2P_{3/2})5d$ (3/2,3/2) 3	$4f^{14}5p^5(^2P_{3/2})6p$ (3/2,1/2) 2	1	bl 542.95
549.28	W VII	5.2e+4	335017 - 517074	$4f^{14}5p^5(^2P_{3/2})5d$ (3/2,3/2) 2	$4f^{14}5p^5(^2P_{3/2})6p$ (3/2,1/2) 1	1	
597.00	W VII	~2.8e+4	382577 - 550082	$4f^{14}5p^5(^2P_{3/2})5d$ (3/2,5/2) 1	$4f^{14}5p^5(^2P_{3/2})6p$ (3/2,3/2) 0	1	bl 2×298.5
605.93	W VI	~3.9e+5	0 - 165037	$5d\ ^2D_{3/2}$	$6p\ ^2P_{3/2}$	5	bl 604.55, 607.56 He II
639.68	W VI	7.8e+5	8709 - 165037	$5d\ ^2D_{5/2}$	$6p\ ^2P_{3/2}$	5	
677.72	W VI	5.7e+5	0 - 147553	$5d\ ^2D_{3/2}$	$6p\ ^2P_{1/2}$	5	
703.38	W VII	~2.8e+4	533693 - 675864	$4f^{13}(^2F_{7/2})5p^6 6p$ (7/2,3/2) 5	$4f^{13}(^2F_{7/2})5p^6 7s$ (7/2,1/2) 4	1	bl 703 O III
707.61	W VII	~1.5e+4	534838 - 676159	$4f^{13}(^2F_{7/2})5p^6 6p$ (7/2,3/2) 3	$4f^{13}(^2F_{7/2})5p^6 7s$ (7/2,1/2) 3	1	sh 703.38
715.19	W VII	~1.2e+4	539127 - 678949	$4f^{14}5p^5(^2P_{3/2})6p$ (3/2,3/2) 3	$4f^{14}5p^5(^2P_{3/2})7s$ (3/2,1/2) 2	1	bl 716.73
716.73	W V	~1.2e+4	6245 - 145768	$5d^2\ ^3F_3$	$5d(^2D_{5/2})6p$ (5/2,3/2) 3	8	bl 715.19, 717.14
717.14	W VII	~1.4e+4	536420 - 675864	$4f^{13}(^2F_{7/2})5p^6 6p$ (7/2,3/2) 4	$4f^{13}(^2F_{7/2})5p^6 7s$ (7/2,1/2) 4	1	bl 716.73
723.88	W V	~1.1e+4	6245 - 144390	$5d^2\ ^3F_3$	$5d(^2D_{5/2})6p$ (5/2,3/2) 2	8	sh 726.17
726.17	W V	1.9e+4	0 - 137709	$5d^2\ ^3F_2$	$5d(^2D_{3/2})6p$ (3/2,3/2) 1	8	
731.73	W V	~2.2e+4	6245 - 142908	$5d^2\ ^3F_3$	$5d(^2D_{5/2})6p$ (5/2,3/2) 4	8	bl 733.56, non-W
733.56	W V	~1.7e+4	12839 - 149160	$5d^2\ ^3P_0$	$5d(^2D_{5/2})6p$ (5/2,3/2) 1	8	bl 731.73, non-W
738.45	W V	1.1e+4	13742 - 149160	$5d^2\ ^1D_2$	$5d(^2D_{5/2})6p$ (5/2,3/2) 1	8	
743.67	W VII	~3.4e+3	517074 - 651542	$4f^{14}5p^5(^2P_{3/2})6p$ (3/2,1/2) 1	$4f^{14}5p^5(^2P_{3/2})6d$ (3/2,3/2) 2	1	sh 744.89
744.89	W V	~1.0e+4	11519 - 145768	$5d^2\ ^3F_4$	$5d(^2D_{5/2})6p$ (5/2,3/2) 3	8	bl 745.97
745.97	W VII	~1.3e+4	530489 - 664543	$4f^{13}(^2F_{5/2})5p^6 6p$ (5/2,1/2) 3	$4f^{13}(^2F_{5/2})5p^6 6d$ (5/2,3/2) 3	1	bl 744.89, 747.87
747.86	W VII	~5.9e+3	512882 - 646596	$4f^{13}(^2F_{7/2})5p^6 6p$ (7/2,1/2) 3	$4f^{13}(^2F_{7/2})5p^6 6d$ (7/2,3/2) 4	1	bl 745.97
751.53	W VII	~1.3e+4	512882 - 645944	$4f^{13}(^2F_{7/2})5p^6 6p$ (7/2,1/2) 3	$4f^{13}(^2F_{7/2})5p^6 6d$ (7/2,3/2) 3	1	bl 752.13
752.13	W VII	~1.4e+4	513640 - 646596	$4f^{13}(^2F_{7/2})5p^6 6p$ (7/2,1/2) 4	$4f^{13}(^2F_{7/2})5p^6 6d$ (7/2,3/2) 4	1	bl 751.53
758.01	W VII	~4.1e+4	530489 - 662413	$4f^{13}(^2F_{5/2})5p^6 6p$ (5/2,1/2) 3	$4f^{13}(^2F_{5/2})5p^6 6d$ (5/2,3/2) 4	1	sh 759.89
759.89	W VII	~1.4e+5	513640 - 645238	$4f^{13}(^2F_{7/2})5p^6 6p$ (7/2,1/2) 4	$4f^{13}(^2F_{7/2})5p^6 6d$ (7/2,3/2) 5	1	bl 760 O V
760.74	W V	~1.9e+5	66658 - 198108	$5d6s\ ^3D_3$	$6s6p\ ^3P_2$	8	bl 760 O V, 761.73
761.73	W VII	~1.6e+5	519194 - 650474	$4f^{14}5p^5(^2P_{3/2})6p$ (3/2,1/2) 2	$4f^{14}5p^5(^2P_{3/2})6d$ (3/2,3/2) 3	1	bl 760.74
775.21	W V	1.2e+4	0 - 128997	$5d^2\ ^3F_2$	$5d(^2D_{5/2})6p$ (5/2,1/2) 2	8	

780.89	W V	~2.1e+4	16331 - 144390	$5d^2\ ^3P_1$	$5d(^2D_{5/2})6p$ (5/2,3/2) 2	8	bl 780 O IV
786.25	W V	~1.4e+5	6245 - 133430	$5d^2\ ^3F_3$	$5d(^2D_{3/2})6p$ (3/2,3/2) 2	8	sh 788.27
797.06	W V	~1.6e+5	60296 - 185757	$5d6s\ ^3D_2$	$6s6p\ ^3P_1$	8	bl 797.65
797.65	W V	~1.6e+5	11519 - 136888	$5d^2\ ^3F_4$	$5d(^2D_{3/2})6p$ (3/2,3/2) 3	8	bl 797.06
806.66	W V	~5.6e+4	13742 - 137709	$5d^2\ ^1D_2$	$5d(^2D_{3/2})6p$ (3/2,3/2) 1	8	sh 810.23
810.23	W V	~2.4e+5	22346 - 145768	$5d^2\ ^1G_4$	$5d(^2D_{5/2})6p$ (5/2,3/2) 3	8	bl 811.46
811.46	W V	~2.1e+5	6245 - 129480	$5d^2\ ^3F_3$	$5d(^2D_{5/2})6p$ (5/2,1/2) 3	8	bl 810.23
814.65	W V	~1.0e+5	6245 - 128997	$5d^2\ ^3F_3$	$5d(^2D_{5/2})6p$ (5/2,1/2) 2	8	sh 811.46
817.49	W V	1.1e+5	0 - 122326	$5d^2\ ^3F_2$	$5d(^2D_{3/2})6p$ (3/2,1/2) 1	8	
821.19	W V	9.4e+4	22615 - 144390	$5d^2\ ^3P_2$	$5d(^2D_{5/2})6p$ (5/2,3/2) 2	8	
823.87	W V	~3.5e+4	16331 - 137709	$5d^2\ ^3P_1$	$5d(^2D_{3/2})6p$ (3/2,3/2) 1	8	sh 821.19
829.45	W V	~1.0e+4	22346 - 142908	$5d^2\ ^1G_4$	$5d(^2D_{5/2})6p$ (5/2,3/2) 4	8	sh 833 O III
835.50	W V	~3.1e+4	13742 - 133430	$5d^2\ ^1D_2$	$5d(^2D_{3/2})6p$ (3/2,3/2) 2	8	bl 835 O III
842.72	W V	1.3e+5	0 - 118663	$5d^2\ ^3F_2$	$5d(^2D_{3/2})6p$ (3/2,1/2) 2	8	
847.74	W V	3.8e+4	11519 - 129480	$5d^2\ ^3F_4$	$5d(^2D_{5/2})6p$ (5/2,1/2) 3	8	
864.78	W VII	~8.0e+4	534838 - 650474	$4f^{13}(^2F_{7/2})5p^6 6p$ (7/2,3/2) 3	$4f^{14}5p^5(^2P_{3/2})6d$ (3/2,3/2) 3	1	bl 865.77
867.64	W V	~4.4e+4	13742 - 128997	$5d^2\ ^1D_2$	$5d(^2D_{5/2})6p$ (5/2,1/2) 2	8	sh 865.77
873.04	W V	~2.4e+4	22346 - 136888	$5d^2\ ^1G_4$	$5d(^2D_{3/2})6p$ (3/2,3/2) 3	8	sh 873.42
873.42	W VII	~3.0e+4	551684 - 666177	$4f^{13}(^2F_{5/2})5p^6 6p$ (5/2,3/2) 4	$4f^{13}(^2F_{5/2})5p^6 6d$ (5/2,5/2) 5	1	sh 874.29
874.29	W VII	~3.9e+4	533693 - 648072	$4f^{13}(^2F_{7/2})5p^6 6p$ (7/2,3/2) 5	$4f^{13}(^2F_{7/2})5p^6 6d$ (7/2,5/2) 6	1	bl 876.11
876.11	W VI	~5.7e+4	147553 - 261695	$6p\ ^2P_{1/2}$	$6d\ ^2D_{3/2}$	5	bl 874.29, 876.20
876.20	W VII	~5.7e+4	534428 - 648558	$4f^{13}(^2F_{7/2})5p^6 6p$ (7/2,3/2) 2	$4f^{13}(^2F_{7/2})5p^6 6d$ (7/2,5/2) 2	1	bl 876.11, 877.60
877.60	W VII	~5.0e+4	536420 - 650367	$4f^{13}(^2F_{7/2})5p^6 6p$ (7/2,3/2) 4	$4f^{13}(^2F_{7/2})5p^6 6d$ (7/2,5/2) 5	1	bl 876.20
885.11	W VII	~2.7e+4	536420 - 649401	$4f^{13}(^2F_{7/2})5p^6 6p$ (7/2,3/2) 4	$4f^{13}(^2F_{7/2})5p^6 6d$ (7/2,5/2) 4	1	sh 887.58
887.58	W V	~3.5e+4	16331 - 128997	$5d^2\ ^3P_1$	$5d(^2D_{5/2})6p$ (5/2,1/2) 2	8	bl 888.70
888.70	W VII	~4.4e+4	543641 - 656165	$4f^{14}5p^5(^2P_{3/2})6p$ (3/2,3/2) 2	$4f^{14}5p^5(^2P_{3/2})6d$ (3/2,5/2) 3	1	bl 887.58
895.60	W IV	~3.1e+4	35094 - 146750	$5d^2(^3F)6s\ ^4F_{5/2}$	$5d(^2D)6s6p(^3P)\ ^2D_{3/2}$	9	bl 895.75
895.75	W IV	~3.1e+4	46088 - 157726	$5d^2(^3P)6s\ ^4P_{5/2}$	$5d(^2D)6s6p(^3P)\ ^2P_{3/2}$	9	bl 895.60, 896.54
896.54	W IV	~2.7e+4	58373 - 169913	$5d^2(^1G)6s\ ^2G_{7/2}$	$5d(^2D)6s6p(^1P)\ ^2D_{5/2}$	9	bl 895.75
904.59	W IV	~1.4e+4	52828 - 163375	$5d^2(^3F)6s\ ^2F_{7/2}$	$5d(^2D)6s6p(^1P)\ ^2F_{5/2}$	9	bl 904 C II
908.22	W IV	~2.7e+4	64681 - 174786	$5d^2(^3P)6s\ ^2P_{3/2}$	$5d(^2D)6s6p(^1P)\ ^2P_{3/2}$	9	bl 910.06
910.06	W IV	~2.8e+4	0 - 109882	$5d^3\ ^4F_{3/2}$	$5d^2(^3P)6p\ ^4S_{3/2}$	9	bl 908.22
933.41	W V	~1.1e+4	22346 - 129480	$5d^2\ ^1G_4$	$5d(^2D_{5/2})6p$ (5/2,1/2) 3	8	bl 933.52
933.52	W IV	~1.1e+4	3537 - 110658	$5d^3\ ^4F_{5/2}$	$5d^2(^1D)6p\ ^2F_{5/2}$	9	bl 933.41, 933.53
933.53	W IV	~1.1e+4	56416 - 163536	$5d^2(^1D)6s\ ^2D_{5/2}$	$5d(^2D)6s6p(^1P)\ ^2D_{3/2}$	9	bl 933.52
935.77	W V	~1.4e+4	22615 - 129480	$5d^2\ ^3P_2$	$5d(^2D_{5/2})6p$ (5/2,1/2) 3	8	bl 935.86
935.86	W IV	~1.4e+4	9256 - 116110	$5d^3\ ^4F_{9/2}$	$5d^2(^3P)6p\ ^4D_{7/2}$	9	bl 935.77
942.95	W V	1.0e+4	43110 - 149160	$5d^2\ ^1S_0$	$5d(^2D_{5/2})6p$ (5/2,3/2) 1	8	
953.10	W V	~8.1e+3	13742 - 118663	$5d^2\ ^1D_2$	$5d(^2D_{3/2})6p$ (3/2,1/2) 2	8	bl 956.6
967.75	W VII	~3.9e+4	446749 - 550082	$4f^{14}5p^5(^2P_{3/2})6s$ (3/2,1/2) 1	$4f^{14}5p^5(^2P_{3/2})6p$ (3/2,3/2) 0	1	bl 967.82
995.98	W VII	~2.2e+4	443237 - 543641	$4f^{14}5p^5(^2P_{3/2})6s$ (3/2,1/2) 2	$4f^{14}5p^5(^2P_{3/2})6p$ (3/2,3/2) 2	1	sh 994.48
1003.86	W IV	~1.4e+4	9256 - 108872	$5d^3\ ^4F_{9/2}$	$5d^2(^1G)6p\ ^2G_{7/2}$	9	sh 1006.29
1006.29	W VI	~3.4e+4	165037 - 264412	$6p\ ^2P_{3/2}$	$6d\ ^2D_{5/2}$	5	bl 1006.66
1007.74	W VII	~3.0e+4	437188 - 536420	$4f^{13}(^2F_{7/2})5p^6 6s$ (7/2,1/2) 4	$4f^{13}(^2F_{7/2})5p^6 6p$ (7/2,3/2) 4	1	bl 1007.07

1009.88	W VII	~8.5e+3	454566 - 553588	$4f^{13}(^2F_{5/2})5p^6 6s$ (5/2,1/2) 2	$4f^{13}(^2F_{5/2})5p^6 6p$ (5/2,3/2) 3	1	sh 1007.74
1019.32	W VII	~1.3e+4	454566 - 552671	$4f^{13}(^2F_{5/2})5p^6 6s$ (5/2,1/2) 2	$4f^{13}(^2F_{5/2})5p^6 6p$ (5/2,3/2) 2	1	sh 1024.07
1024.07	W VII	~7.3e+4	437188 - 534838	$4f^{13}(^2F_{7/2})5p^6 6s$ (7/2,1/2) 4	$4f^{13}(^2F_{7/2})5p^6 6p$ (7/2,3/2) 3	1	bl 1025.14
1025.14	W IV	~8.6e+4	24096 - 121644	$5d^3\ ^2G_{9/2}$	$5d^2(^1D)6p\ ^2F_{7/2}$	9	bl 1024.07, 1025.44 D I
1032.08	W VII	~1.9e+4	446749 - 543641	$4f^{14}5p^5(^2P_{3/2})6s$ (3/2,1/2) 1	$4f^{14}5p^5(^2P_{3/2})6p$ (3/2,3/2) 2	1	bl 1031.91 O VI, 1032.93
1032.93	W VII	~1.7e+4	438026 - 534838	$4f^{13}(^2F_{7/2})5p^6 6s$ (7/2,1/2) 3	$4f^{13}(^2F_{7/2})5p^6 6p$ (7/2,3/2) 3	1	bl 1032.08
1036.21	W VII	~2.8e+4	437188 - 533693	$4f^{13}(^2F_{7/2})5p^6 6s$ (7/2,1/2) 4	$4f^{13}(^2F_{7/2})5p^6 6p$ (7/2,3/2) 5	1	bl 1036.57
1036.57	W IV	~3.0e+4	6745 - 103217	$5d^3\ ^4F_{7/2}$	$5d^2(^3F)6p\ ^4D_{5/2}$	9	bl 1036.21, 1036.66
1036.66	W VII	~3.0e+4	455221 - 551684	$4f^{13}(^2F_{5/2})5p^6 6s$ (5/2,1/2) 3	$4f^{13}(^2F_{5/2})5p^6 6p$ (5/2,3/2) 4	1	bl 1036.57, 1037.33
1037.33	W VII	~3.3e+4	438026 - 534428	$4f^{13}(^2F_{7/2})5p^6 6s$ (7/2,1/2) 3	$4f^{13}(^2F_{7/2})5p^6 6p$ (7/2,3/2) 2	1	bl 1036.66, 1037.61 O VI
1041.15	W V	~2.1e+4	22615 - 118663	$5d^2\ ^3P_2$	$5d(^2D_{3/2})6p$ (3/2,1/2) 2	8	bl 1041.59
1041.59	W IV	~2.2e+4	9256 - 105263	$5d^3\ ^4F_{9/2}$	$5d^2(^3F)6p\ ^4F_{9/2}$	9	bl 1041.15, 1042.87
1042.87	W VII	~2.1e+4	443237 - 539127	$4f^{14}5p^5(^2P_{3/2})6s$ (3/2,1/2) 2	$4f^{14}5p^5(^2P_{3/2})6p$ (3/2,3/2) 3	1	bl 1041.59
1049.20	W IV	~2.9e+4	16205 - 111515	$5d^3\ ^2H_{9/2}$	$5d^2(^3F)6p\ ^4D_{7/2}$	9	sh 1046.50
1049.33	W VII	~2.9e+4	454566 - 549865	$4f^{13}(^2F_{5/2})5p^6 6s$ (5/2,1/2) 2	$4f^{13}(^2F_{5/2})5p^6 6p$ (5/2,3/2) 1	1	sh 1046.50
1050.93	W IV	~1.3e+4	3537 - 98692	$5d^3\ ^4F_{5/2}$	$5d^2(^3P)6p\ ^4D_{5/2}$	9	sh 1050.67
1068.25	W IV	~2.2e+4	9256 - 102868	$5d^3\ ^4F_{9/2}$	$5d^2(^3F)6p\ ^2F_{7/2}$	9	bl 1068.25
1068.25	W IV	~2.2e+4	15261 - 108872	$5d^3\ ^2G_{7/2}$	$5d^2(^1G)6p\ ^2G_{7/2}$	9	bl 1068.25, 1068.63
1068.63	W IV	~2.2e+4	6745 - 100322	$5d^3\ ^4F_{7/2}$	$5d^2(^3F)6p\ ^4F_{7/2}$	9	bl 1068.25
1072.96	W IV	~9.8e+3	22223 - 115423	$5d^3\ ^2H_{11/2}$	$5d^2(^3F)6p\ ^2G_{9/2}$	9	bl 1074.70
1088.03	W IV	4.7e+3	11773 - 103682	$5d^3\ ^4P_{1/2}$	$5d^2(^3F)6p\ ^4D_{1/2}$	9	
1099.05	W IV	~5.3e+3	3537 - 94525	$5d^3\ ^4F_{5/2}$	$5d^2(^3F)6p\ ^4F_{5/2}$	9	bl 1098.65
1108.29	W IV	~1.4e+4	10221 - 100450	$5d^3\ ^4P_{3/2}$	$5d^2(^3F)6p\ ^2D_{3/2}$	9	bl 1107.4, 1108.8
1119.72	W IV	6.7e+3	3537 - 92846	$5d^3\ ^4F_{5/2}$	$5d^2(^3F)6p\ ^4G_{7/2}$	9	
1125.31	W V	7.8e+3	60296 - 149160	$5d6s\ ^3D_2$	$5d(^2D_{5/2})6p$ (5/2,3/2) 1	8	
1135.15	W IV	~7.5e+3	11773 - 99867	$5d^3\ ^4P_{1/2}$	$5d^2(^1D)6p\ ^2D_{3/2}$	9	sh 1137.1
1137.1	W VIII	1.5e+4	1233 - 89123	$4f^{14}5p^5\ ^2P_{3/2}$	$4f^{14}5p^5\ ^2P_{1/2}$		±0.5, M1, NIST 1137.79
1147.90	W IV	5.7e+3	22766 - 109882	$5d^3\ ^2D2_{5/2}$	$5d^2(^3P)6p\ ^4S_{3/2}$	9	
1161.36	W IV	~1.2e+4	47680 - 133785	$5d^2(^3P)6s\ ^4P_{3/2}$	$5d(^2D)6s6p(^3P)\ ^4F_{5/2}$	9	bl 1161.37, 1159.8
1161.37	W IV	~1.2e+4	22766 - 108872	$5d^3\ ^2D2_{5/2}$	$5d^2(^1G)6p\ ^2G_{7/2}$	9	bl 1161.36
1164.47	W V	~4.2e+3	58514 - 144390	$5d6s\ ^3D_1$	$5d(^2D_{5/2})6p$ (5/2,3/2) 2	8	sh 1168.15
1168.15	W VI	~5.0e+4	79431 - 165037	$6s\ ^2S_{1/2}$	$6p\ ^2P_{3/2}$	5	bl 1168.67 He I
1172.47	W IV	~5.8e+3	0 - 85290	$5d^3\ ^4F_{3/2}$	$5d^2(^3F)6p\ ^4G_{5/2}$	9	sh 1176 C III
1189.14	W V	3.6e+3	60296 - 144390	$5d6s\ ^3D_2$	$5d(^2D_{5/2})6p$ (5/2,3/2) 2	8	
1225.69	W IV	2.2e+3	25168 - 106754	$5d^3\ ^2P_{3/2}$	$5d^2(^3F)6p\ ^2F_{5/2}$	9	
1232.37	W VII	6.4e+4	462496 - 543641	$4f^{14}5p^5(^2P_{1/2})5d$ (1/2,3/2) 1	$4f^{14}5p^5(^2P_{3/2})6p$ (3/2,3/2) 2	1	
1238.58	W V	3.8e+4	58514 - 139252	$5d6s\ ^3D_1$	$5d(^2D_{3/2})6p$ (3/2,3/2) 0	8	
1255.14	W IV	~1.2e+4	10221 - 89893	$5d^3\ ^4P_{3/2}$	$5d^2(^3F)6p\ ^4F_{3/2}$	9	sh 1259.46 O V
1308.01	W VII	7.6e+4	437188 - 513640	$4f^{13}(^2F_{7/2})5p^6 6s$ (7/2,1/2) 4	$4f^{13}(^2F_{7/2})5p^6 6p$ (7/2,1/2) 4	1	
1321.11	W VII	~2.8e+4	437188 - 512882	$4f^{13}(^2F_{7/2})5p^6 6s$ (7/2,1/2) 4	$4f^{13}(^2F_{7/2})5p^6 6p$ (7/2,1/2) 3	1	bl 1322.50
1322.50	W VII	~2.8e+4	438026 - 513640	$4f^{13}(^2F_{7/2})5p^6 6s$ (7/2,1/2) 3	$4f^{13}(^2F_{7/2})5p^6 6p$ (7/2,1/2) 4	1	bl 1321.11

bl - blend sh - line on shoulder

References 1 – Sugar and Kaufman, 1975 5 – Sugar and Kaufman, 1979 7 – Kildiyarova *et al*., 1996
8 – Meijer, 1986 9 – Iglesias *et al*., 1985

Table 3. Leading contributing states to the $4f^{12}5p^{6}5d_{5/2}$ and $4f^{12}5p^{6}5d_{7/2}$ W VIII levels

Configuration and Term	Energy (cm^{-1})	Leading contributing state with percentage	Second contributing state with percentage
$4f^{12}5p^{6}5d_{5/2}$	409676	23% $4f^{12}(^{3}F_{4})5p^{6}5d$ (4,3/2)	22% $4f^{12}(^{3}H_{4})5p^{6}5d$ (4,3/2)
	411819	18% $4f^{13}5p^{5}(5/2,3/2)_{4}5d$ (4,5/2)	11% $4f^{12}(^{3}H_{5})5p^{6}5d$ (5,5/2)
	415852	20% $4f^{12}(^{3}F_{2})5p^{6}5d$ (2,3/2)	14% $4f^{12}(^{3}F_{3})5p^{6}5d$ (3,3/2)
	424781	23% $4f^{12}(^{3}H_{4})5p^{6}5d$ (4,5/2)	8% $4f^{12}(^{1}G_{4})5p^{6}5d$ (4,3/2)
	432963	17% $4f^{12}(^{3}P_{2})5p^{6}5d$ (2,3/2)	16% $4f^{14}5p^{4}(^{1}D_{2})5d$ (2,3/2)
	445286	15% $4f^{12}(^{1}D_{2})5p^{6}5d$ (2,5/2)	14% $4f^{13}5p^{5}(7/2,1/2)_{3}5d$ (3,3/2)
	447909	16% $4f^{12}(^{1}G_{4})5p^{6}5d$ (4,5/2)	14% $4f^{12}(^{3}F_{2})5p^{6}5d$ (2,5/2)
	466219	20% $4f^{12}(^{3}P_{2})5p^{6}5d$ (2,5/2)	15% $4f^{13}5p^{5}(5/2,1/2)_{2}5d$ (2,3/2)
	468034	28% $4f^{13}5p^{5}(5/2,1/2)_{2}5d$ (2,3/2)	20% $4f^{12}(^{3}P_{1})5p^{6}5d$ (1,5/2)
$4f^{12}5p^{6}5d_{7/2}$	393992	20% $4f^{12}(^{3}H_{6})5p^{6}5d$ (6,5/2)	19% $4f^{13}5p^{5}(7/2,3/2)_{5}5d$ (5,5/2)
	408086	25% $4f^{12}(^{3}H_{6})5p^{6}5d$ (6,5/2)	23% $4f^{12}(^{3}H_{5})5p^{6}5d$ (5,3/2)
	410654	20% $4f^{12}(^{3}H_{5})5p^{6}5d$ (5,5/2)	16% $4f^{12}(^{3}F_{4})5p^{6}5d$ (4,5/2)
	411832	22% $4f^{12}(^{3}F_{2})5p^{6}5d$ (2,3/2)	18% $4f^{12}(^{3}F_{4})5p^{6}5d$ (4,3/2)
	428777	19% $4f^{12}(^{3}H_{4})5p^{6}5d$ (4,3/2)	16% $4f^{12}(^{3}F_{2})5p^{6}5d$ (2,5/2)
	430708	24% $4f^{12}(^{1}G_{4})5p^{6}5d$ (4,5/2)	21% $4f^{12}(^{3}F_{3})5p^{6}5d$ (3,5/2)

Table 4. Unidentified W lines observed with the short wavelength high resolution detector

Wavelength (Å)	Intensity	Comments	Wavelength (Å)	Intensity	Comments
148.1	1.4e+5		282.1	1.9e+5	
156.0	5.1e+4		285.1	~1.6e+5	sh 284.16 Fe XV
164.3	~1.4e+5	sh 165.37	286.0	~8.7e+4	sh 285.1
173.7	1.3e+5		287.8	3.1e+5	
177.5	7.4e+4		290.5	~3.1e+5	sh 289.53
178.2	~8.7e+4	sh 179.27 Ni XV	296.0	2.6e+5	
182.6	~9.0e+4	sh 183.49 Cu XVII	297.6	~1.4e+5	sh 298.5
186.8	1.0e+5		298.5	4.4e+5	
191.0	~6.6e+4	sh 192.03 Fe XXIV	300.8	1.3e+5	
194.65	~2.4e+5	W VIII (10), bl 194.53	307.2	7.4e+4	
204.49	~2.8e+5	W VIII (10), sh 205.22	308.1	2.4e+5	
207.99	~5.3e+5	W VIII (10), bl 208.42	309.6	1.7e+5	
210.2	1.6e+5		312.1	~8.4e+4	bl 312.43 C IV
219.46	4.7e+5	W VI (10)	313.6	~5.7e+4	W VI T, bl 313.58
221.45	~1.6e+5	W VI (10), bl 221.44	316.2	5.7e+4	
222.05	~2.6e+5	W VI (10), bl 221.92	318.0	1.0e+5	
222.88	7.4e+5	W VI (10)	322.9	8.4e+4	
226.1	4.1e+5		333.3	~1.7e+5	bl 332.84
236.2	1.3e+5		334.9	~1.5e+5	bl 334.31, 335.41 Fe XVI
238.6	~4.1e+5	W VI (10), bl 239.09	341.8	1.7e+5	
243.7	9.0e+4		342.5	~7.9e+4	sh 341.77

247.2	~1.2e+5	sh 246.36	347.3	4.7e+4	
267.8	1.8e+5	W VI (10)	349.6	3.5e+4	
268.6	2.0e+5	W VI (10)	353.0	5.9e+4	
269.8	3.9e+5	W VI (10)	368.8	4.3e+4	
271.1	~6.7e+4	bl 271.7	374.4	4.2e+4	
271.7	~7.4e+4	bl 271.1	377.7	2.6e+4	
272.9	1.9e+5		389.5	~7.0e+4	bl 389.86 Cr XIV
274.4	8.8e+5	W VI (10)	405.0	1.9e+4	
275.0	~3.9e+5	sh 274.4	414.3	2.4e+4	
276.2	3.5e+5	W VI (10)	416.2	2.2e+4	
278.3	6.4e+4		421.6	9.9e+3	
278.9	9.9e+4		424.7	~3.8e+4	bl 423.6, 425.5
279.5	1.0e+5		425.5	~3.0e+4	sh 424.7
280.7	~6.0e+4	sh 281.47 Ni XVII T			

The accuracy of the wavelengths of unblended lines is ±0.2 Å
bl - blend sh - line on shoulder T - tentative
References 10 – Clementson *et al*., 2015

Table 5. Unidentified W lines observed with the long wavelength lower resolution detector

Wavelength (Å)	Intensity	Comments	Wavelength (Å)	Intensity	Comments
553.1	2.5e+4		1056.0	5.3e+3	
616.6	2.9e+4	W VII - W VIII	1064.5	5.2e+3	
625.3	~4.5e+4	sh 627.16	1081.2	1.1e+4	W VII - W VIII
649.1	3.0e+4	W VII - W VIII	1107.8	~1.5e+4	bl 1108.29
659.6	1.8e+4	W IV - W VI	1159.5	1.7e+4	W VII - W VIII
956.6	1.3e+4	W VII - W VIII	1177.8	2.4e+4	W VII - W VIII
961.1	9.4e+3	W VII - W VIII	1183.4	3.1e+3	
970.8	~2.9e+4	bl 968.95	1200.2	2.3e+3	
987.6	5.6e+3				

The accuracy of the wavelengths of unblended lines is ±1.0 Å
bl - blend sh - line on shoulder T - tentative

4. Dependence of the W emission on plasma parameters

The spectral analysis has been carried out for a pulse in which a significant W influx occurred leading to one of the most extensive spectrum of low temperature W features. Such influxes can occur at any time during plasma operations, either when the plasma is close enough to interact with a surface on which W has been previously deposited or when W dust particles enter the plasma.

In addition to these occasional influxes, the W spectral lines are seen mainly during ELMy H-mode discharges. In these cases, the intensity of the W emission depends on plasma parameters, in particular the plasma configuration being used, the plasma temperature and the ELMs themselves. Of particular interest is an ELMy H-mode pulse, number 94607, whose plasma parameters are shown in figure 13.

Figure 14 shows that in this pulse the W VII emission, given by the time history of the 261.39 Å line observed with the short wavelength VUV detector (KT7/2), coincides with the ELMs as indicated by the D_α emission. In the time window illustrated in figure 14 the ELM frequency is ~12 s^{-1}, although the D_α signal shows that the ELMs are compound. The 4008.8 Å, W I emission, recorded with a near-UV/visible spectrometer, known locally as KT3, is also shown in this diagram. KT3 uses a mirror system to view the plasma (Meigs *et al.*, 2010) and its time vector is chosen to be at the centre of its 40 ms integration window. Its lines of sight, together with those of the KS3 spectrometer used to observe the D_α emission, are shown in figure 15. This pulse is of interest in that not only are the ELMs slow enough to be correlated with the KT3 and KT7 spectroscopic signals, which have a more limited time resolution, but the outer strike point moves from the more central horizontal tile 5 to the corner tile 6 at 12 s. The magnetic configurations are illustrated in figure 16. Before 12 s the strongest ELM behaviour is observed in the divertor volume, whereas after this time signals viewing the bottom of the outer wall and the outer divertor throat show enhanced behaviour associated with the ELMs. Figure 17 shows the vertical D-alpha emission which views the bottom of the outer wall and the divertor D-alpha, measured with a line of sight directly into the divertor. The most intense W VII signals occur during the later phase suggesting that the W observed by the KT7/2 spectrometer is being released from close to the divertor throat rather than the horizontal W tiles within the divertor. Measurements of the W I emission observed by KT3 which views the outer divertor throat would support this conclusion (figure 18).

More usually the ELM frequency is higher than in pulse 94607 as a result of the higher gas puffing needed both for W control and to support high power neutral beam operation so that individual ELMs cannot be resolved on the time resolution of the spectrometers and a time averaged W intensity must be used. In the ELMy H-mode pulses a correlation is found with the ELM frequency, particularly so for ELMs of an intermediate size. This can be seen in figure 19, which shows the dependency of the W VII, 261.39 Å line intensity on ELM frequency for 36 pulses in the pulse range 94440 to 95520. Although all these pulses are in the ELMy H-mode regime, they represent a range of plasma parameters, toroidal fields from 1.7 to 3.4 T, plasma currents from 1.4 to 3 MA, maximum T_e and n_e from 3.2 to 7.7 keV and 1.6 to 9.0×10^{19} m^{-3}, respectively, with total additional heating from 8 to 29 MW. The additional heating is by neutral beam injection (NBI) and ion cyclotron resonance heating (ICRH). The W VII intensities are averaged over a period of 0.25 s with the intermediate ELMs being defined as having vertical D-alpha intensities, averaged over this period, of between 1.0 and 4.0×10^{14} ph/s.cm^2.sr. Large ELMs are seen to have a weak dependence, while small ELMs, although still leading to significant W VII release, show no particular dependence on the ELM frequency.

Two other dependences are illustrated in figure 20, those on the main chamber temperature and on the distance of the plasma from the vessel wall and divertor throat. This figure shows the results of an analysis of 56 ELMy H-mode pulses in the range 94440 to 95528, with the same wide ranges of plasma parameters, the W VII intensities again being averaged over a period of 0.25 s. It is clear that the highest

W intensities can only be achieved if the plasma temperature is also high, this resulting in more energetic particles impacting on the divertor throat. The temperature is measured using high resolution Thompson scattering at a major radius of 3.7m, close to the pedestal region, but still within the core plasma. Given that the release mechanism depends on a number of parameters, a high temperature does not automatically result in a high intensity. For example, pulses which have a smaller plasma-divertor throat gap tend to have higher W VII intensities. The blue points in figure 20 have a plasma-wall gap (measured from a point R = 3.33 m, z = -1.07 m on the wall surface) of less than 15 mm whereas this parameter is greater than 15 mm for the red points, which generally have lower W VII intensities.

The question also arises as to whether the W released from the divertor throat reaches the core plasma. Figure 21 shows the results of an analysis of 55 pulses in the range 94440 to 95520 in which the core W concentration is plotted as a function of the W VII line intensity. As before averaging is carried out over intervals of 0.25 s. Although W reaching the core plasma will originate from a number of different surfaces, it is seen that high W VII intensities ensure a minimum core concentration. This suggests that the W released from the divertor throat does make a contribution to the core W inventory. The core W concentration is determined using the W analyzer, although it is noted that the same result is obtained by determining the W level from the intensities of higher temperature W spectral features emitted from the JET main chamber. The application of W analyzer method on ASDEX is described by Pütterich *et al*. (2008).

5. Electron temperature and concentration estimates

The observation of discrete lines from low ionization stages of W allows quantitative measurements of W to be made in the JET divertor. This complements the use of other low temperature spectral features, which in the VUV spectral region involve unresolved transition arrays. These arrays are emitted from somewhat higher temperature regions and correspond to a number of ionization stages that overlap making any quantitative analysis extremely complex. Using discrete lines, electron temperatures of the emitting plasma regions are estimated from W VI and W VII line intensity ratios and absolutely calibrated line intensities from these ionization stages are used to derive estimates of W concentrations. Both of these calculations depend on the available atomic data and this is expected to be the limiting factor in the present analyses. As already noted, the atomic data do not show a density dependence at most densities of interest, $\sim 10^{19\text{-}20}$ m^{-3}, although at the highest divertor densities of $\sim 10^{21}$ m^{-3} a small density sensitivity is expected.

5.1. Electron temperature estimates

Atomic data in the form of Photon Emission Coefficients (PECs) are taken from the OPEN-ADAS files ‘pec40#w_ic#w5.dat’ and ‘pec40#w_ic#w6.dat’ for W VI and W VII, respectively (Summers, 2004). The observed lines that are of sufficient intensity to be useful for these measurements are listed in tables 6 and 7, respectively. For both stages, PECs are available for four of these transitions. The file

'pec40#w_ls#w6.dat' gave alternative data for the W VII, 216.22 and 223.84 Å transitions. However, these data did not alter the final results significantly, typically 1% or less, and, consequently, the results presented here use only 'pec40#w_ic#w6.dat' data.

Since the PECs are listed as functions of both electron temperature and density the data at a density of $10^{19\text{-}20}$ m^{-3} were used and polynomial fits made as a function of temperature. The line intensity for a transition from level *i* to level *j* is given by

$$I_{ij} = n_e n_g \varepsilon_{ij} ,$$

where n_e and n_g are the electron and ground state density of the ionization stage and ε_{ij} is the PEC for transition *i* to *j*. In determining the electron temperature of the plasma region of the W emission, it is more accurate to take line intensity ratios, since this immediately removes the direct dependence on n_e and n_g. In the case of W VI, intensity ratios were taken with the 639.68 Å line and for W VII with the 261.39 Å line intensity. The IDL Constrained_Min routine was then used to minimize the RMS fractional difference between the theoretical and measured ratios in order to obtain an electron temperature of the emitting plasma region for each ionization stage. This procedure is described in more detail by Lawson *et al*. (2011).

Table 6. W VI spectral lines useful for temperature and concentration analyses

Wavelength (Å)	Identification	Comment
222.88	-	High resolution detector. Line neighbouring 223.84 Å W VII line. Line profile fit required. No atomic data.
382.15	$5s^25p^65d\ ^2D_{3/2} - 5s^25p^65f\ ^2F_{5/2}$	High resolution detector.
394.13	$5s^25p^65d\ ^2D_{5/2} - 5s^25p^65f\ ^2F_{7/2}$	High resolution detector.
639.68	$5s^25p^65d\ ^2D_{5/2} - 5s^25p^66p\ ^2P_{3/2}$	Low resolution detector.
677.72	$5s^25p^65d\ ^2D_{3/2} - 5s^25p^66p\ ^2P_{1/2}$	Low resolution detector.

An analysis was carried out for four pulses. The first, pulse 94605, had a sudden, large influx at 14.1 s, which bolometry shows originates at the bottom of the inner wall of the machine close to the inner divertor throat, the intensity rapidly decaying (within ~20 ms). The high intensity ensured a well-defined W spectrum for the analysis. The influx occurred during an ELMy H-mode phase, although the background levels of W on either side of the influx were low as is illustrated in figure 22. This figure shows the line intensity of W VII at 261.39 Å both for this pulse and for the other pulses analysed. The plasma parameters for pulse 94605 are shown in figure 23. There was concern that the transient nature of the influx might affect the results and therefore three other pulses were analysed in which the emission was longer lasting. In pulse 94645 the W emission peaked at 8.2 s during a period of very rapid ELMs, but decayed over a period of 1.6 s, the ELMS continuing but with a lower frequency as can be seen in figure 24. This figure shows the ELM behaviour as indicated by the visible D_α emission, together with

other plasma parameters. In pulses 95460 and 95463 the ELMs were more regular during a period lasting for 4 s. The plasma parameters for these pulses are shown in figure 25.

Table 7. W VII spectral lines useful for temperature and concentration analyses

Wavelength (Å)	Identification	Comment
188.16	$4f^{14}5p^6\ ^1S_0 - 4f^{14}5p^5(^2P_{1/2})6s\ (1/2,1/2)\ 1$	High resolution detector. No atomic data.
216.22	$4f^{14}5p^6\ ^1S_0 - 4f^{14}5p^5(^2P_{1/2})5d\ (1/2,3/2)\ 1$	High resolution detector. Intense line.
223.84	$4f^{14}5p^6\ ^1S_0 - 4f^{14}5p^5(^2P_{3/2})6s\ (3/2,1/2)\ 1$	High resolution detector. Line neighbouring 222.88 Å W VI line. Line profile fit required.
261.39	$4f^{14}5p^6\ ^1S_0 - 4f^{14}5p^5(^2P_{3/2})5d\ (3/2,5/2)\ 1$	High resolution detector. Intense line, dominating blend with 261.77 and 261.85 Å W VIII lines.
289.53	$4f^{14}5p^6\ ^1S_0 - 4f^{13}(^2F_{5/2})5p^6 5d\ (5/2,5/2)\ 1$	High resolution detector. Dominates unidentified line on shoulder at 290.5 Å. No atomic data.
294.37	$4f^{14}5p^6\ ^1S_0 - 4f^{13}(^2F_{5/2})5p^6 5d\ (5/2,3/2)\ 1$	High resolution detector. No atomic data.
302.28	$4f^{14}5p^6\ ^1S_0 - 4f^{13}(^2F_{7/2})5p^6 5d\ (7/2,5/2)\ 1$	High resolution detector. No atomic data.
313.58	$4f^{14}5p^6\ ^1S_0 - 4f^{14}5p^5(^2P_{3/2})5d\ (3/2,3/2)\ 1$	High resolution detector. Line blended with lower temperature W line (possibly W VI).

Details of the analysis are given in tables 8 and 9 for W VI and W VII, respectively. In the case of W VI, measurements are taken from both the short (high resolution) and long wavelength (low resolution) detectors. In pulses 94645, 95460 and 95463, which have a weaker spectrum than that of pulse 94605, line profile fits were carried out to the 677.72 Å line, which is close to the O II line at 672.95 Å. Electron temperatures of between 3.4 to 4.0 eV are obtained with RMS fractional differences of the theoretical and measured line intensity ratios of between 0.07 and 0.17. W VII involved measurements from only the high resolution spectrometer. Despite the better resolution, the proximity of the 222.88 Å W VI line to the 223.84 Å W VII line meant that line profile fitting to these lines was again necessary for a reliable intensity. In both cases, the line profile fitting was achieved with a simple double Gaussian fit, the integration subsequently being carried out with the ±3 or ±5 pixel method applied to the fitted line profiles to ensure the integrity of the absolute sensitivity calibration. As can be seen in table 9, the theoretical 313.58 Å / 261.39 Å line ratio is significantly smaller than the measurement, suggesting that the 313.58 Å line is blended. Consequently, the 313.58 Å line was excluded from the minimization. An electron temperature of the plasma region emitting W VII of between 9.0 and 9.7 eV was calculated, although with significantly larger RMS fractional differences of up to 0.4. A check was made to see how sensitive the results were to the line profile fit of the 223.84 Å line. Taking a 223.84 Å / 261.39 Å ratio 50% lower in the case of pulse 95463 reduced the RMS fractional difference to less than 0.2 but only reduced the derived temperature by 0.11 eV. This demonstrates that the derived temperature depends mainly on the 216.22 Å / 261.39 Å ratio, both lines being intense and therefore providing the most reliable

measurements for this ionization stage. Indeed, using just the ratio of these two intense lines, results in a T_e that is lower by no more than 1.5 eV from the result of the minimization involving the three lines.

Table 8. Electron temperature analyses of the W VI spectrum

Pulse	94605 14.095 s	94645 8.2-8.3 s	95460 7.1-8.8 s	95463 7.3-8.6 s
Wavelength (Å)	Measured line intensity (Ph/s.m^2.sr)			
222.88	9.58×10^{18}	2.41×10^{18}	4.24×10^{18}	3.48×10^{18}
382.15	2.47×10^{19}	5.94×10^{18}	5.15×10^{18}	4.99×10^{18}
394.13	3.90×10^{19}	7.45×10^{18}	9.39×10^{18}	8.87×10^{18}
639.68	6.72×10^{20}	2.14×10^{20}	1.54×10^{20}	1.51×10^{20}
677.72	5.47×10^{20}	1.76×10^{20}	1.33×10^{20}	1.21×10^{20}
Wavelength (Å)	Measured line intensity ratio to 639.68 Å line			
222.88	0.0143	0.0112	0.0276	0.0231
382.15	0.0368	0.0277	0.0335	0.0331
394.13	0.0580	0.0348	0.0612	0.0589
677.72	0.8137	0.8194	0.8638	0.8054
Wavelength (Å)	Theoretical line intensity ratio to 639.68 Å line			
382.15	0.0368	0.0244	0.0357	0.0352
394.13	0.0595	0.0393	0.0577	0.0568
677.72	0.9355	0.9984	0.9400	0.9423
	RMS fractional difference of theoretical from measured line intensity ratios			
	0.0877	0.1619	0.0713	0.1064
	Electron temperature of W VI plasma emitting region (eV)			
	3.93	3.46	3.89	3.87

For both ionization stages considered the derived temperatures are very similar within the ionization stage, covering a range of no more than 0.7 eV, with that measured during the influx in pulse 94605 not being exceptional. This contrasts with the results for C IV in which the temperature of the emitting plasma had a comparatively wide range of temperatures, from 27 to 42 eV for the H-mode phases of a pulse (Lawson *et al.,* 2011). By using only the 216.22 Å / 261.39 Å ratio it is possible to follow the evolution of the temperature during a pulse and also to check the similarity of the derived temperatures for a wide range of pulses. Applying this analysis to 30 measurements in 15 different pulses a mean T_e of 7.98 eV (±4.1%) is found. The closeness of these results is thought due to the narrow temperature range of the plasma in which the ionization stage exists, there being a significant number of stages falling in the temperature range of the divertor plasma. Figure 26 shows the time histories of the temperatures

derived for pulses 95457, 95458 and 95460 using only these two W VII lines. These data do not indicate any strong temperature difference in the plasmas emitting the W VII radiation, despite the core electron temperatures varying between a maximum of 5 and 8 keV, as can be seen in figures 25 and 27. It is noted that in pulse 95457 there is a clear L-H transition at 4.68 s, seen in the D-alpha signal, despite the subsequent high frequency ELMs being so small that there is no clear bolometric signal.

The derived temperatures presented above are much lower than would be expected from the ionization potentials for W VI and W VII of 64.8 and 122.0 eV, respectively (Clementson *et al*., 2010) and would be typical of plasma regions lower in the divertor than close to the divertor throat. Although higher ionization stages can be seen in some pulses, features from W IV to W VIII are typical of many of the spectra analysed. These features might therefore be expected to be emitted from the region close to the W source. If this is the divertor throat, this would also point to higher temperatures for the emitting plasma than those derived in this analysis. It is noted that neighbouring low temperature W ionization stages might also be expected to have temperatures closer to one another than those derived. The results depend on the accuracy of the atomic data used and should be regarded as estimates. Nevertheless, this analysis illustrates the information that can be obtained from the spectrum and will provide interesting comparisons when improved atomic data become available.

Table 9. Electron temperature analyses of the W VII spectrum

Pulse	94605 14.095 s	94645 8.2-8.3 s	95460 7.1-8.8 s	95463 7.3-8.6 s
Wavelength (Å)	Measured line intensity (Ph/s.m^2.sr)			
188.16	5.50×10^{18}	-	-	-
216.22	8.80×10^{19}	2.70×10^{19}	2.57×10^{19}	2.46×10^{19}
223.84	1.30×10^{19}	5.88×10^{18}	5.96×10^{18}	5.81×10^{18}
261.39	8.46×10^{19}	2.64×10^{19}	2.62×10^{19}	2.53×10^{19}
289.53	1.98×10^{19}	-	-	-
294.37	3.76×10^{19}	2.15×10^{19}	1.89×10^{19}	1.80×10^{19}
302.28	3.12×10^{19}	8.55×10^{18}	7.16×10^{18}	7.40×10^{18}
313.58	2.41×10^{19}	2.74×10^{18}	3.98×10^{18}	4.23×10^{18}
Wavelength (Å)	Measured line intensity ratio to 261.39 Å line			
188.16	0.0650	-	-	-
216.22	1.0397	1.0235	0.9805	0.9739
223.84	0.1535	0.2229	0.2277	0.2295
289.53	0.2339	-	-	-
294.37	0.4436	0.8161	0.7209	0.7119
302.28	0.3686	0.3243	0.2735	0.2923

313.58	0.2851	0.1038	0.1520	0.1672
Wavelength (Å)	Theoretical line intensity ratio to 261.39 Å line			
216.22	1.2540	1.2289	1.1697	1.1602
223.84	0.0889	0.0871	0.0829	0.0822
313.58	0.0171	0.0168	0.0160	0.0158
	RMS fractional difference of theoretical from measured line intensity ratios			
	0.2705	0.3704	0.3837	0.3867
	Electron temperature of W VII plasma emitting region (eV)			
	9.68	9.50	9.09	9.03
	Temperature of W VII plasma emitting region using only 216 and 261 Å lines (eV)			
	8.25	8.15	7.90	7.86

5.2. W concentration estimates

The availability of an absolute sensitivity calibration for the VUV spectrometers allows the concentration of W in the spectrometer's line of sight to be determined. This is given by

$$c_W = \frac{4\pi I_{ij}}{n_e^2 l \varepsilon_{ij}}$$

where l is the path length over which the W emission is emitted. In this instance only an illustrative calculation is presented. An electron density of 10^{20} m^{-3} is chosen together with a path length of 0.1 m. ε_{ij} at the temperature determined by the minimization is used. The concentration estimates for W VI and W VII are given in tables 10 and 11, respectively, and are found to be significantly higher than would be expected (for example, main chamber W concentrations are shown in figure 21). This is particularly so when it is remembered that in pulse 94605 the W is released from the *inner* wall or divertor throat, but is observed along a line-of-sight viewing the outer divertor. A higher electron density closer to 10^{21} m^{-3} is required to reduce the W VII estimates to values comparable to the main chamber concentrations, but would still be insufficient for the W VI estimates. However, the derived concentrations are found to be sensitive to the electron temperature of the emitting plasma region through the value of the PEC used, particularly in the case of W VI. For this ionization stage doubling T_e reduces the concentrations by up to ×50. Such a change would bring the estimates from the two ionization stages into closer agreement. As discussed in section 5.1, the limiting factor for the derivation of the temperatures is the atomic data used, again emphasizing the need for the most accurate atomic data.

Table 10. Concentration analyses of the W VI spectrum

Pulse	94605 14.095 s	94645 8.2-8.3 s	95460 7.1-8.8 s	95463 7.3-8.6 s
Wavelength (Å)	Measured line intensity (Ph/s.m^2.sr)			

382.15	2.47×10^{19}	5.94×10^{18}	5.15×10^{18}	4.99×10^{18}
394.13	3.90×10^{19}	7.45×10^{18}	9.39×10^{18}	8.87×10^{18}
639.68	6.72×10^{20}	2.14×10^{20}	1.54×10^{20}	1.51×10^{20}
677.72	5.47×10^{20}	1.76×10^{20}	1.33×10^{20}	1.21×10^{20}
	Electron temperature of W VI plasma emitting region (eV)			
	3.93	3.46	3.89	3.87
	W concentration estimate from W VI line intensities			
382.15	1.13×10^{-1}	7.83×10^{-2}	2.54×10^{-2}	2.56×10^{-2}
394.13	1.10×10^{-1}	6.11×10^{-2}	2.87×10^{-2}	2.82×10^{-2}
639.68	1.13×10^{-1}	6.90×10^{-2}	2.71×10^{-2}	2.72×10^{-2}
677.72	9.82×10^{-2}	5.66×10^{-2}	2.49×10^{-2}	2.33×10^{-2}

Table 11. Concentration analyses of the W VII spectrum

Pulse	94605 14.095 s	94645 8.2-8.3 s	95460 7.1-8.8 s	95463 7.3-8.6 s
Wavelength (Å)	Measured line intensity (Ph/s.m^2.sr)			
216.22	8.80×10^{19}	2.70×10^{19}	2.57×10^{19}	2.46×10^{19}
223.84	1.30×10^{19}	5.88×10^{18}	5.96×10^{18}	5.81×10^{18}
261.39	8.46×10^{19}	2.64×10^{19}	2.62×10^{19}	2.53×10^{19}
	Electron temperature of W VII plasma emitting region (eV)			
	9.68	9.50	9.09	9.03
	W concentration estimate from W VII line intensities			
216.22	2.77×10^{-3}	9.42×10^{-4}	1.15×10^{-3}	1.15×10^{-3}
223.84	5.77×10^{-3}	2.89×10^{-3}	3.78×10^{-3}	3.84×10^{-3}
261.39	3.34×10^{-3}	1.13×10^{-3}	1.38×10^{-3}	1.38×10^{-3}

6. Conclusions

An extensive analysis is presented of a low temperature VUV W spectrum recorded in the JET plasma that shows discrete spectral lines. The spectrum analysed has W IV to W VIII features and includes the first observation in the VUV of a magnetic dipole transition from a low ionization stage of W. These results should provide the necessary information to enable the low temperature VUV spectral features to be used for diagnostic purposes, in particular showing the likely blends in these complex spectra and, consequently, the required spectral resolution. The analysis also highlights where additional line identifications and atomic data are needed.

ELMy H-mode plasmas are found to be most efficient at releasing the observed W with ELMs of frequency ~100 s^{-1} leading to the highest W levels. The source of the W is shown to be predominately

the divertor throat and evidence showing that this W contributes to the core W inventory is presented. Both the electron temperature of the core plasma and the plasma – wall separation are found to affect the W levels observed in the VUV spectra.

Illustrative calculations of the electron temperature of the plasma regions emitting W VI and W VII lines are given, together with concentration estimates. The electron temperatures are found to be very similar from pulse to pulse and do not vary significantly during a pulse, typically being ~4 and 9 eV for the W VI and W VII ionization stages, respectively. This is significantly lower than the ionization potentials of 64.8 and 122.0 eV for these stages and would be lower than expected if the observed W is released from the divertor throat. The reproducibility of the measured temperatures suggests a very limited region of emission, which would be consistent with the large number of W ionization stages occurring at low temperatures. The derived concentrations are regarded as being unrealistically high and emphasize the need for the highest quality atomic data for reliable measurements of these parameters.

This work has been carried out within the framework of the EUROfusion Consortium and has received funding from the Euratom research and training programme 2014-2018 and 2019-2020 under grant agreement No 633053 and from the RCUK Energy Programme [grant number EP/I501045]. The views and opinions expressed herein do not necessarily reflect those of the European Commission.

References

Angioni C *et al.*, 2014, Nucl. Fusion, **54**, 083028
Angioni C *et al.*, 2016, Proc. 26th IAEA Fusion Energy Conference, Kyoto, Japan
Ballance C P *et al.,* 2013, J. Phys. B, **46**, 055202
Casson F J *et al.*, 2020, Nucl. Fusion, **60**, 066029
Churilov S S *et al*., 1996, Can. J. Phys., 74, 145 (https://doi.org/10.1139/p96-023)
Clementson J *et al.,* 2010, J. Phys. B, **43**, 144009
Clementson J *et al*., 2015, Atoms, **3**, 407
Coenen J W *et al*., 2015, J. Nucl. Mater., **463**, 78
Deprince J and Quinet P, 2015, Atoms, **3**, 299 (https://doi.org/10.3390/atoms3030299)
Dong C F *et al*., 2019, Nucl. Fusion, **59**, 016020
Dux R *et al*., 2011, Nucl. Fusion, **51**, 053002
Fonck R J *et al*., 1982, Appl. Opt., **21** 2115
Iglesias L *et al*., 1985, Phys. Scr., **31**, 173 (https://doi.org/10.1088/0031-8949/31/3/004)
Iglesias L *et al*., 1989, J. Res. Natl. Inst. Stand. Technol., **94**, 221 (https://doi.org/10.6028/jres.094.023)
Kildiyarova R R *et al*., 1996, Phys. Scr., **53**, 454 (https://doi.org/10.1088/0031-8949/53/4/007)
Kramida A *et al*., 2020, NIST Atomic Spectra Database (ver. 5.8), https://physics.nist.gov/asd (https://doi.org/10.18434/T4W30F)
Lawson K D *et al*., 1987, Report TAN(87)1-3, 'Validation of KT2 data and the SAS, spectroscopic database'
Lawson K D and Peacock N J, 1988, Opt. Commun., **68**, 121
Lawson K D *et al.*, 2011, Plasma Phys. Control. Fusion, **53**, 015002
Lawson K D *et al.*, 2021, In preparation
Loarte A *et al.*, 2007, Nucl. Fusion, **47**, S203
Matthews G F *et al.*, 2007, Phy. Scr., **T128**, 137
Meigs A *et al.*, 2010, Rev. Sci. Instrum., **81**, 10E532 (https://doi.org/10.1063/1.3502322)
Meijer F G, 1986, Physica B+C, **141**, 230 (https://doi.org/10.1016/0378-4363(86)90277-9)
Mita M et al., 2017, J. Phys.: Conf. Ser, **875**, 012019
Oishi T *et al*., 2016, Phys. Scr., **91**, 025602
Pawelec E *et al*., 2017, Proc. 44th EPS Conf., Belfast, UK
Pütterich T *et al.* 2008, Plasma Phys. Control. Fusion, **50**, 085016
Ryabtsev A N *et al*., 2013, Phys. Scr., **87**, 045303 (https://doi.org/10.1088/0031-8949/87/04/045303)
Ryabtsev A N *et al*., 2015, Atoms, **3**, 273
Schwob J L *et al*., 1987, Rev. Sci. Instrum., **58**, 1601
Sugar J and Kaufman V, 1975, Phys. Rev. A **12**, 994, (https://doi.org/10.1103/PhysRevA.12.994)
Sugar J and Kaufman V, 1979, J. Opt. Soc. Am., **69**, 141, (https://doi/10.1364/JOSA.69.000141)
Summers H P, 2004, The ADAS User Manual, version 2.6, 2004, https://open.adas.ac.uk
Thorman A *et al,* 2021, To be submitted to Phys. Scr.
Valisa M *et al.*, 2016, Proc. 26th IAEA Fusion Energy Conference, Kyoto, Japan
van Rooij G J *et al*., 2013, J. Nucl. Mater., **438**, S42
Wolf R C *et al*., 1995, JET Preprint, JET-P(95) 34
Wyart J-F *et al*., 1981, Phys. Scr., **23**, 1069 (https://doi.org/10.1088/0031-8949/23/6/008)
Yang X *et al.*, 2020, Nucl. Fusion, **60**, 086012
**See author list of E. Joffrin et al., 2018, 27th Fusion Energy Conf. (Ahmedabad, India, Oct. 2018)*

Diagrams

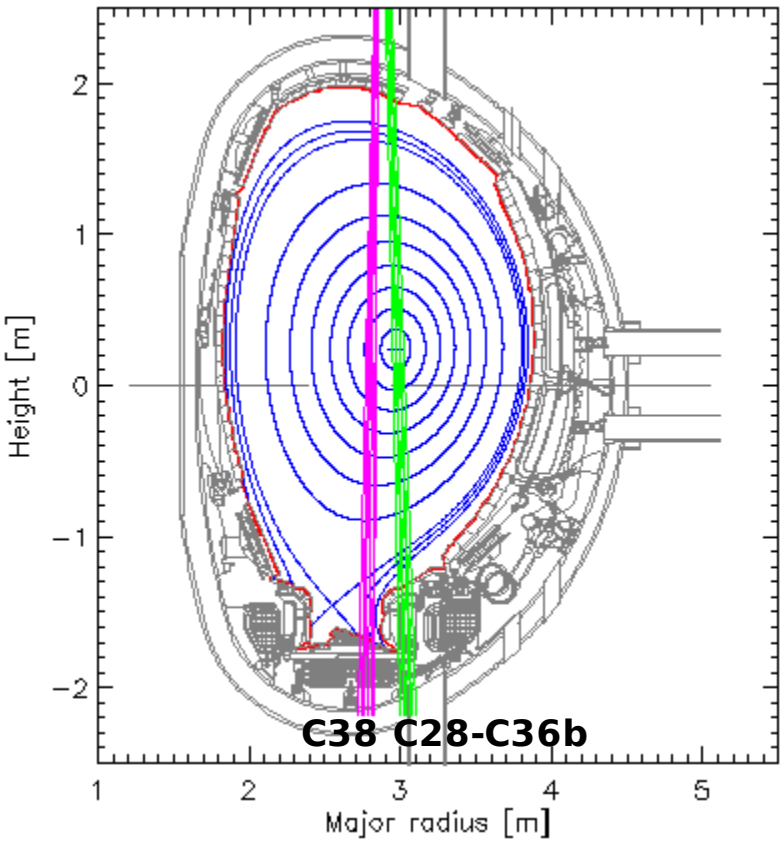

Figure 1. Lines-of-sight of the VUV spectrometer during the different JET-ILW campaigns, also showing the magnetic configuration at 11 s in pulse 94607. All data presented (except pulse 90271 in figures 2 and 3) from C38 campaign.

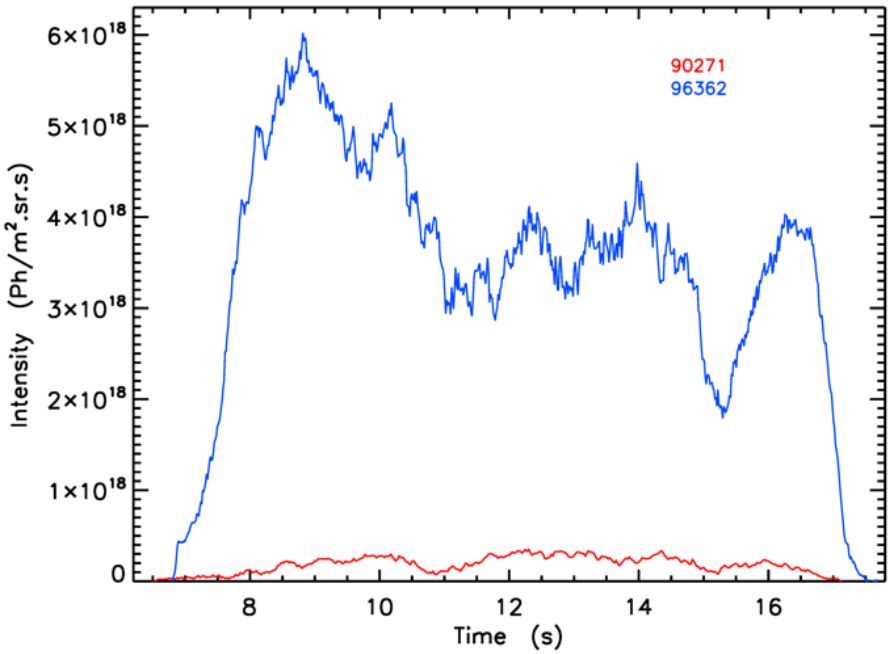

Figure 2. Time histories of the W VII, 261.39 Å line intensity in hybrid scenario pulses 90271 and 96362. Note that pulse 96362 had marginally higher NBI and ICRH heating powers as shown in figure 3.

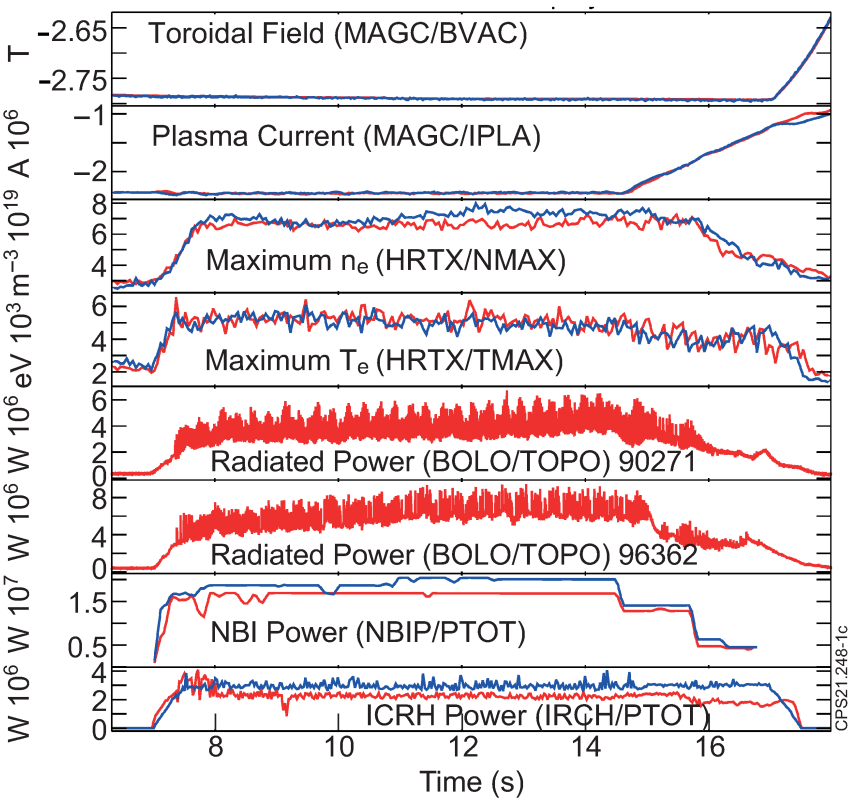

Figure 3. Plasma parameters for pulses 90271 (in red) and 96362 (except for radiated power in blue).

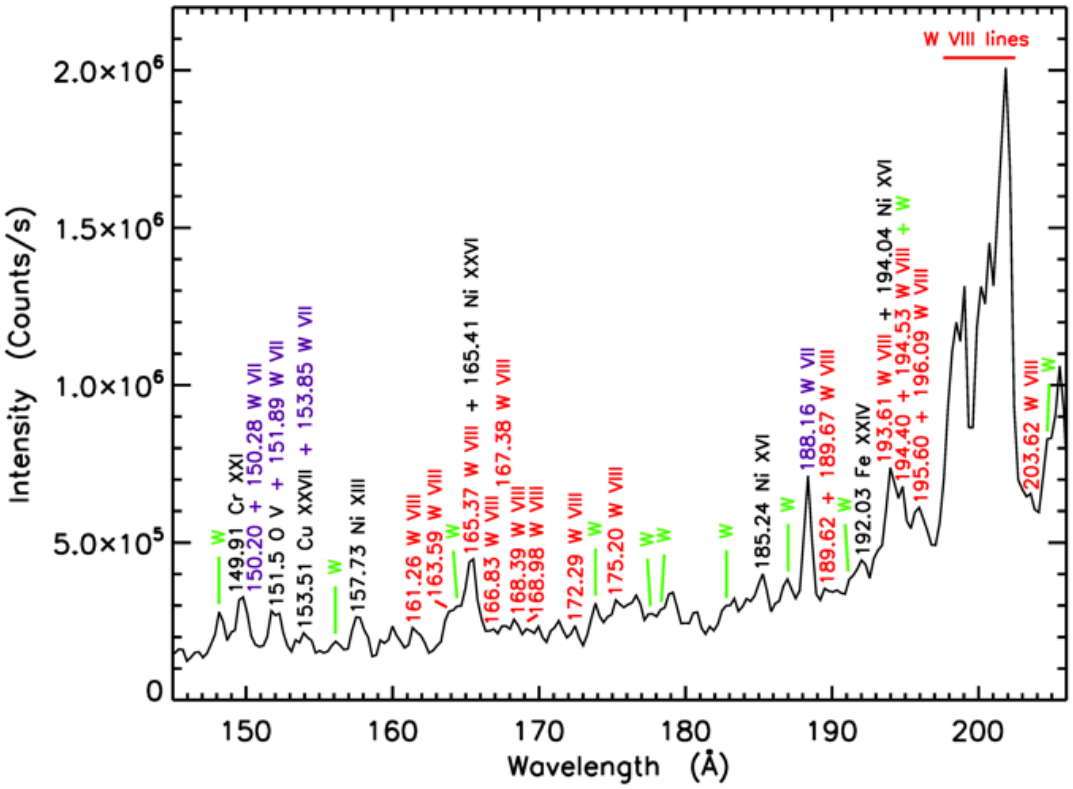

Figure 4a. Spectrum of pulse 95012 during a large influx at 54.37 s covering a wavelength range of 145 to 206 Å.

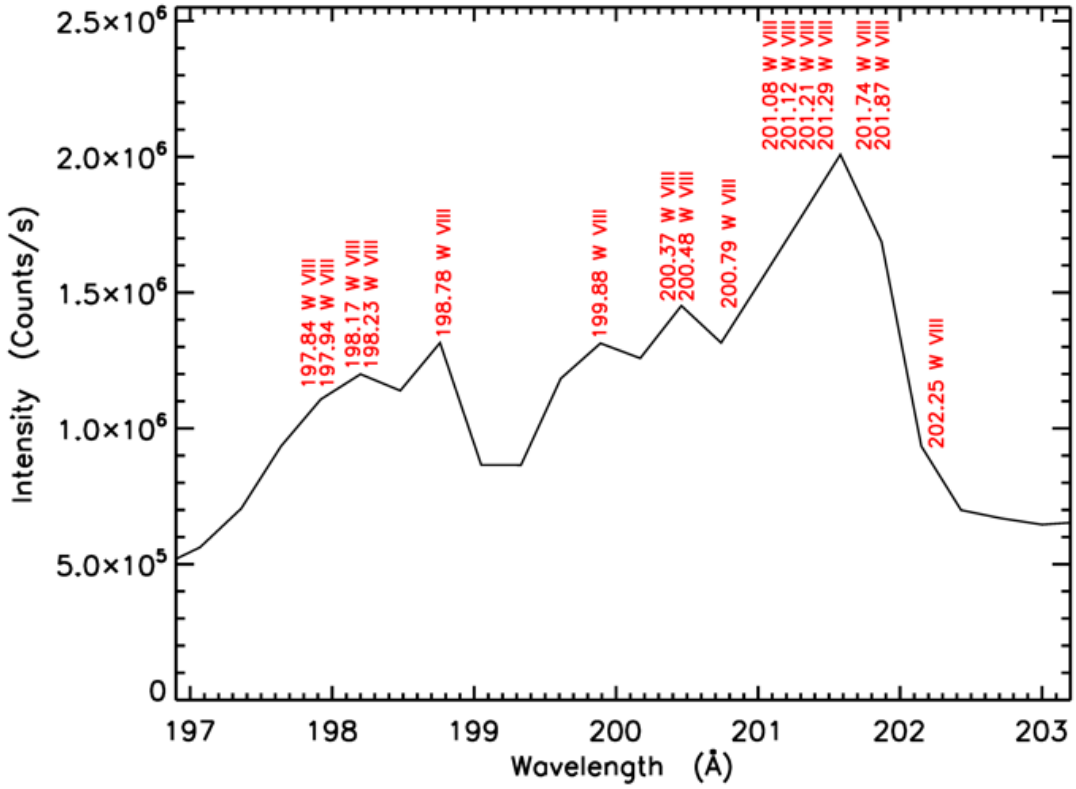

Figure 4b. Spectrum of pulse 95012 during a large influx at 54.37 s covering a wavelength range of 197 to 203 Å.

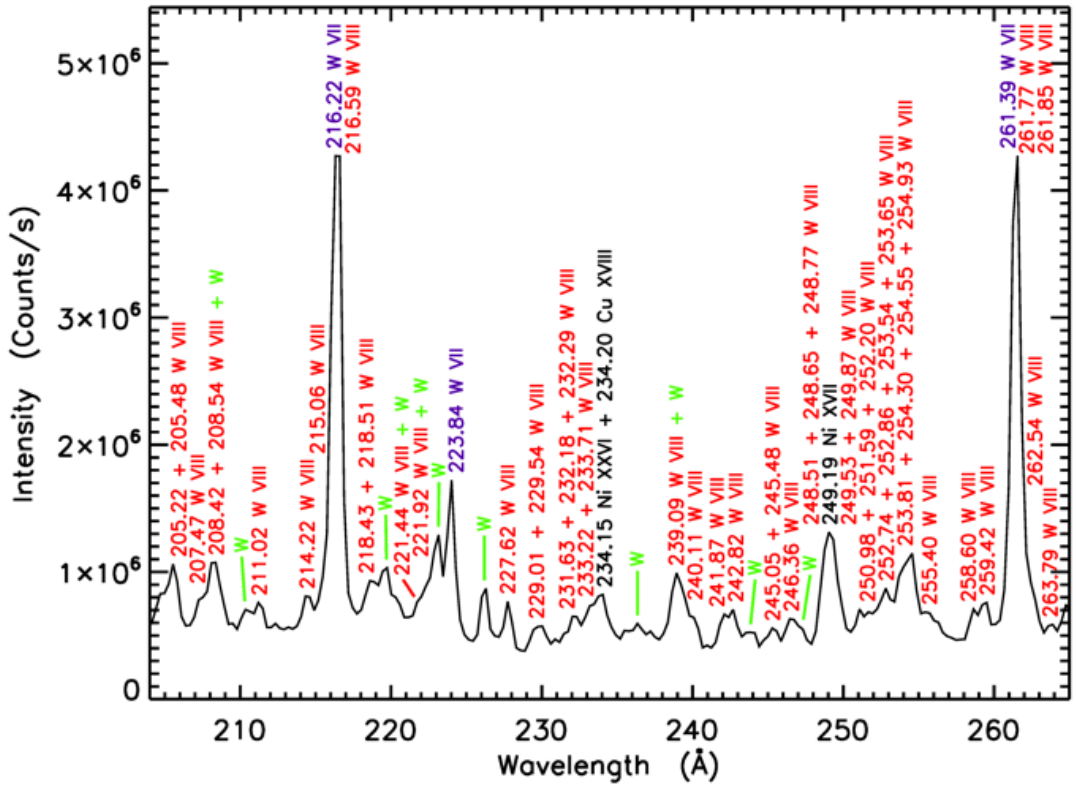

Figure 5. Spectrum of pulse 95012 during a large influx at 54.37 s covering a wavelength range of 204 to 265 Å.

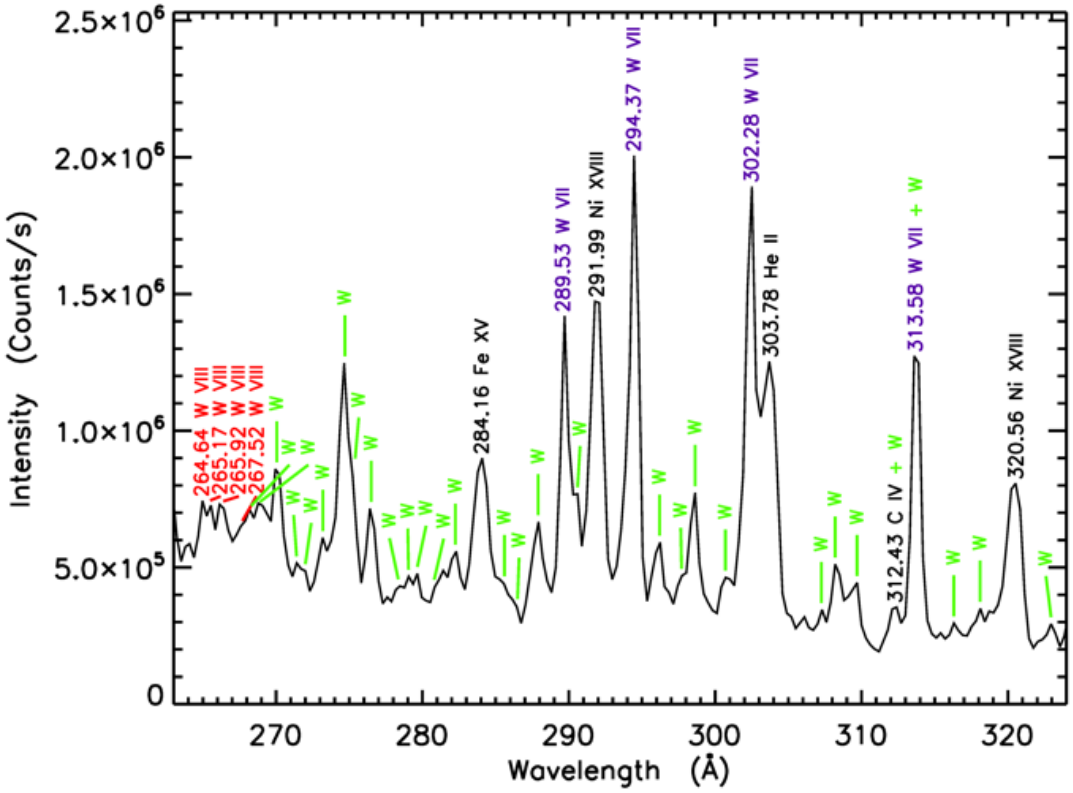

Figure 6. Spectrum of pulse 95012 during a large influx at 54.37 s covering a wavelength range of 263 to 324 Å.

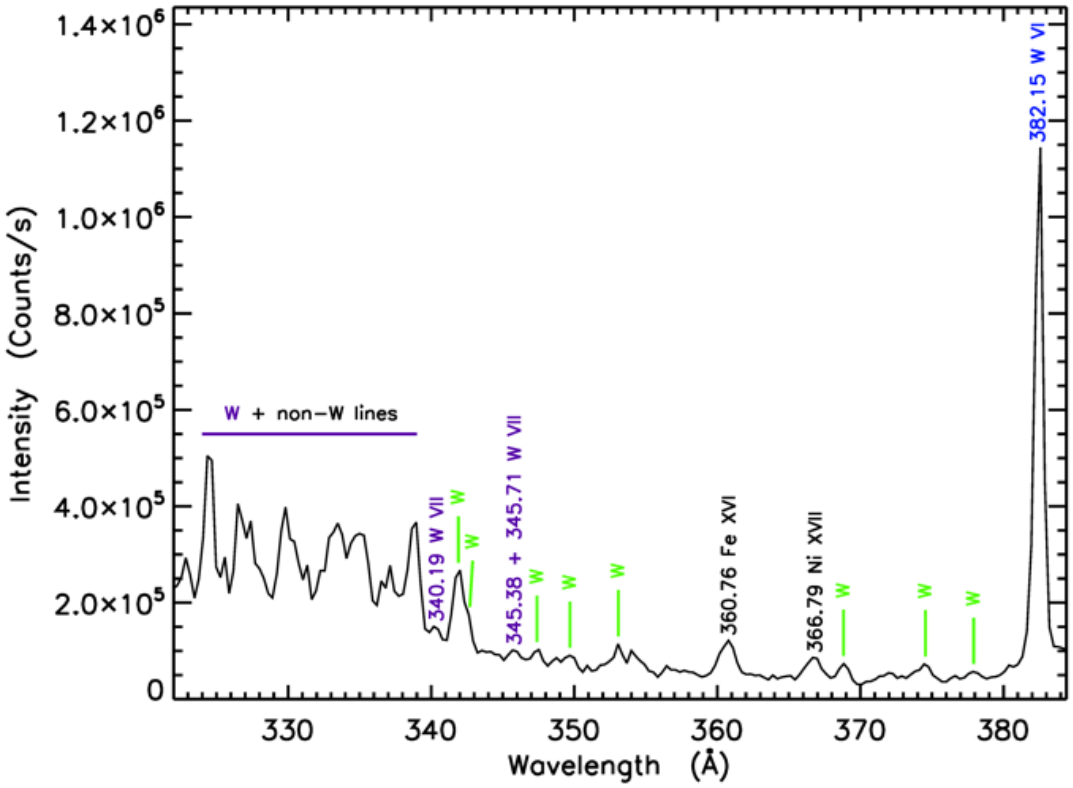

Figure 7a. Spectrum of pulse 95012 during a large influx at 54.37 s covering a wavelength range of 322 to 384 Å.

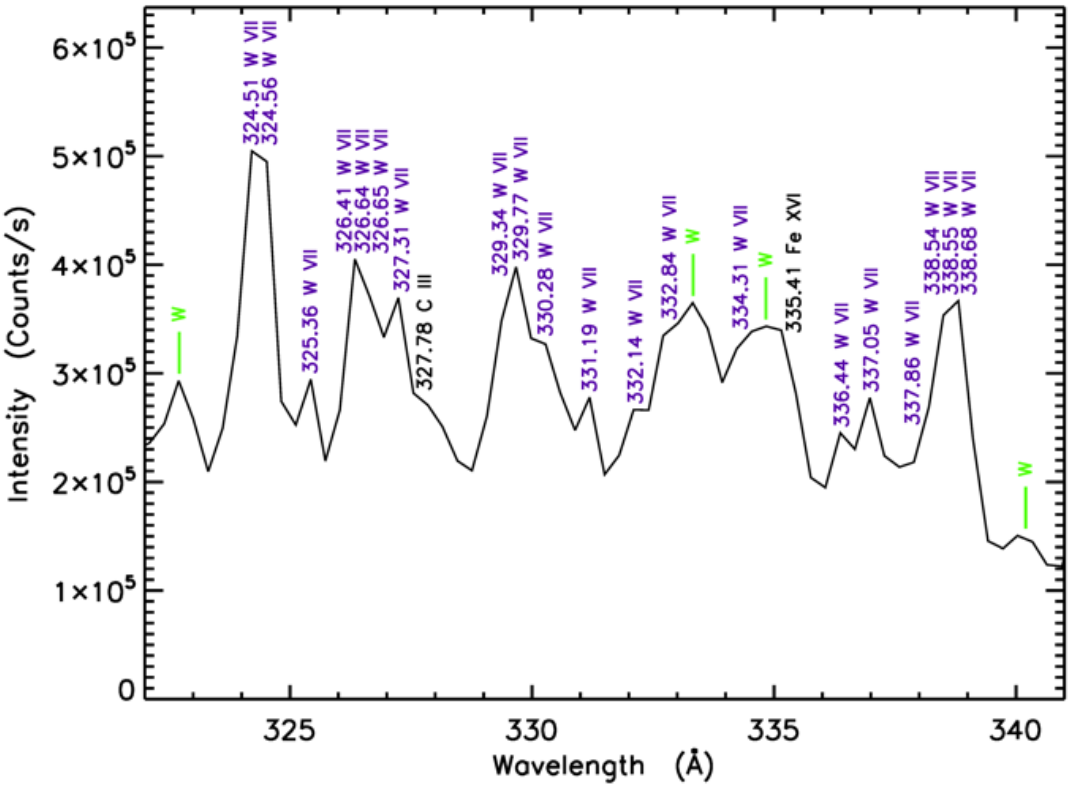

Figure 7b. Spectrum of pulse 95012 during a large influx at 54.37 s covering a wavelength range of 322 to 341 Å.

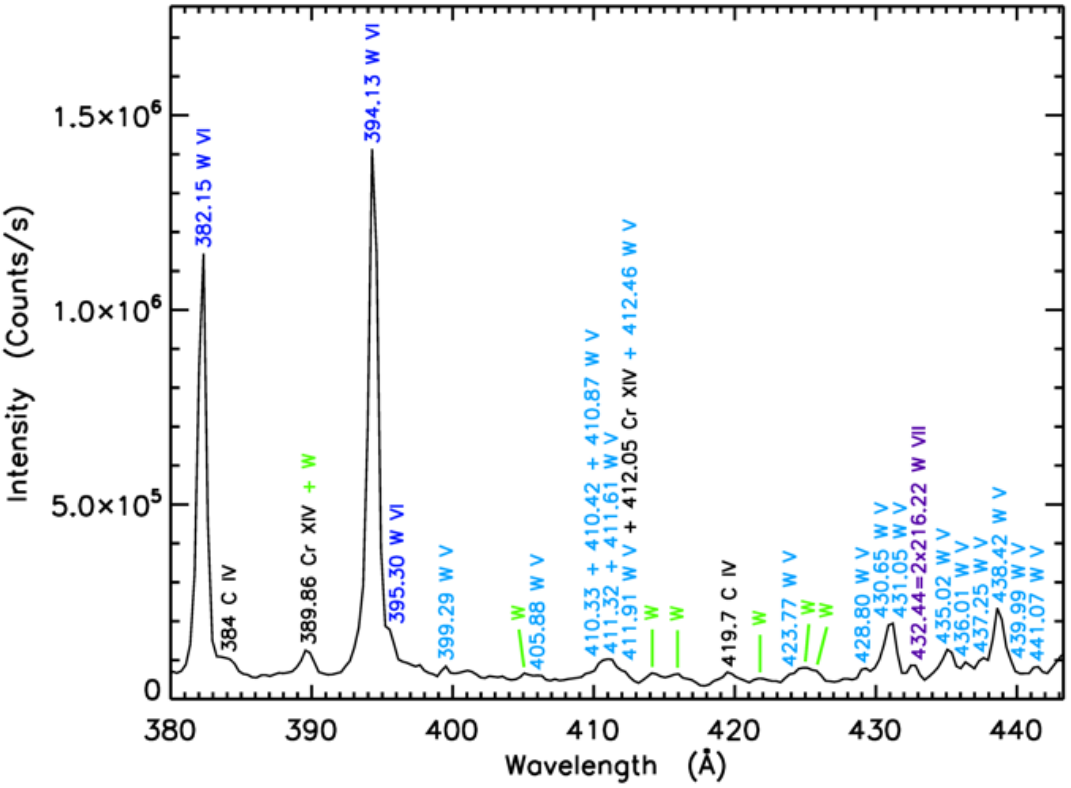

Figure 8. Spectrum of pulse 95012 during a large influx at 54.37 s covering a wavelength range of 380 to 443 Å.

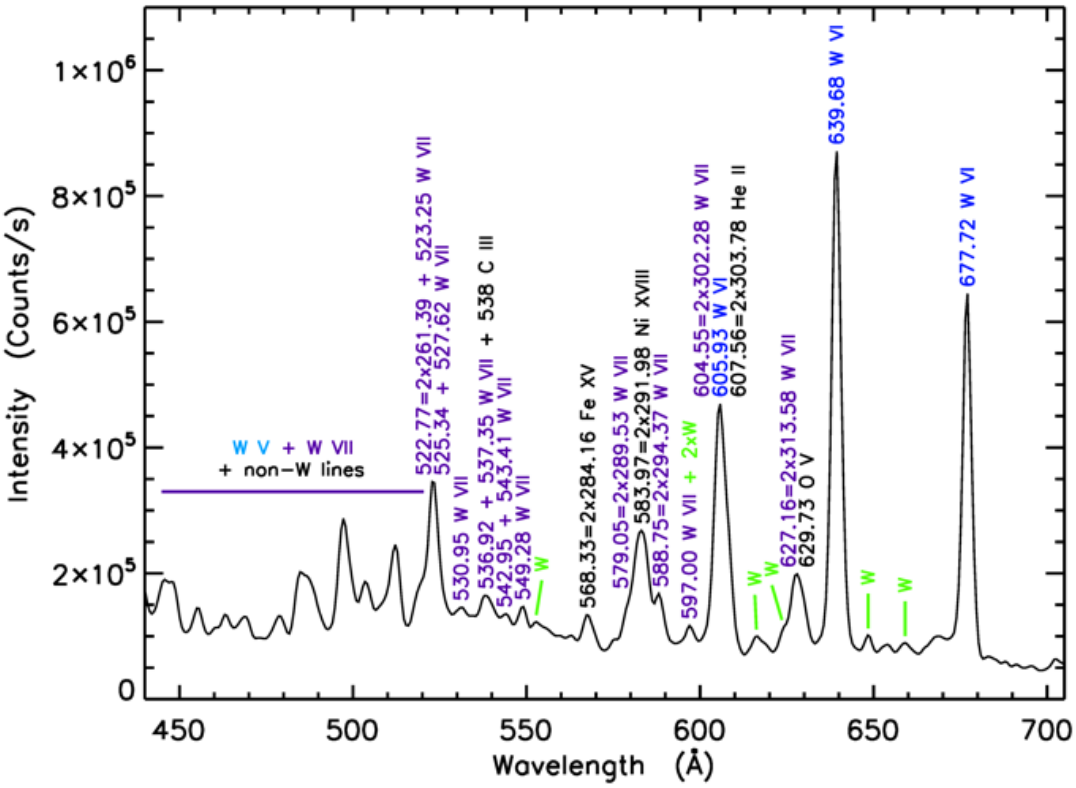

Figure 9a. Spectrum of pulse 95012 during a large influx at 54.37 s covering a wavelength range of 440 to 705 Å.

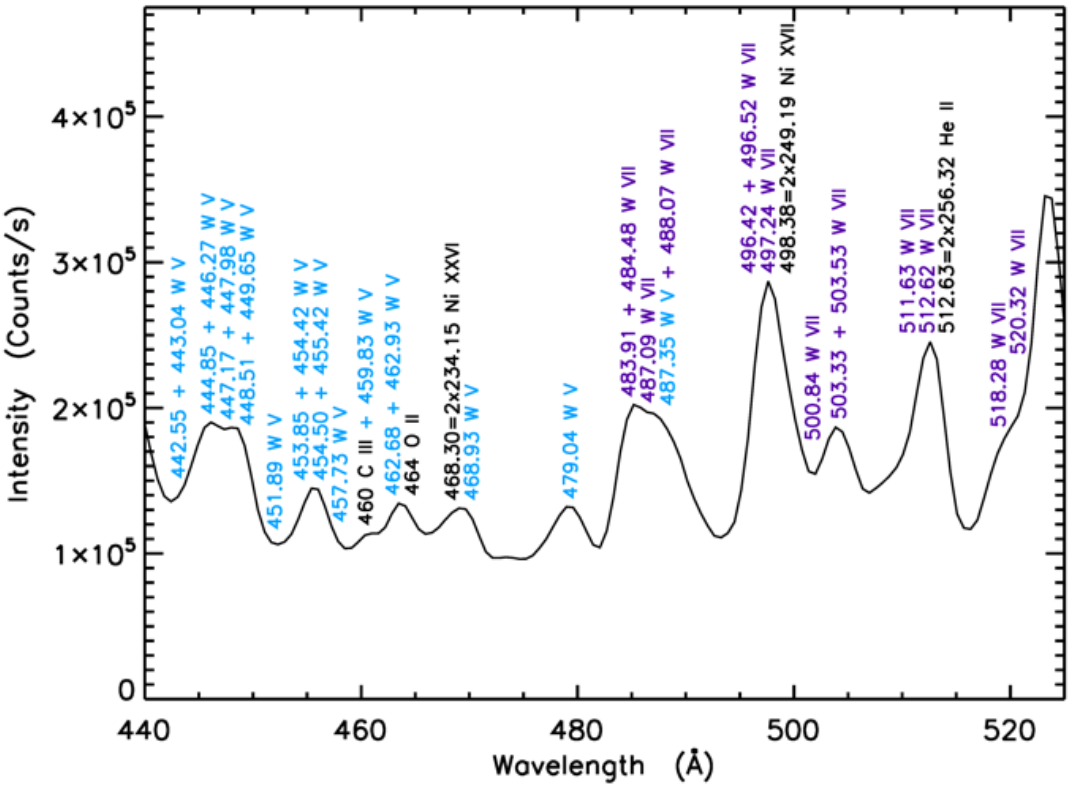

Figure 9b. Spectrum of pulse 95012 during a large influx at 54.37 s covering a wavelength range of 440 to 525 Å.

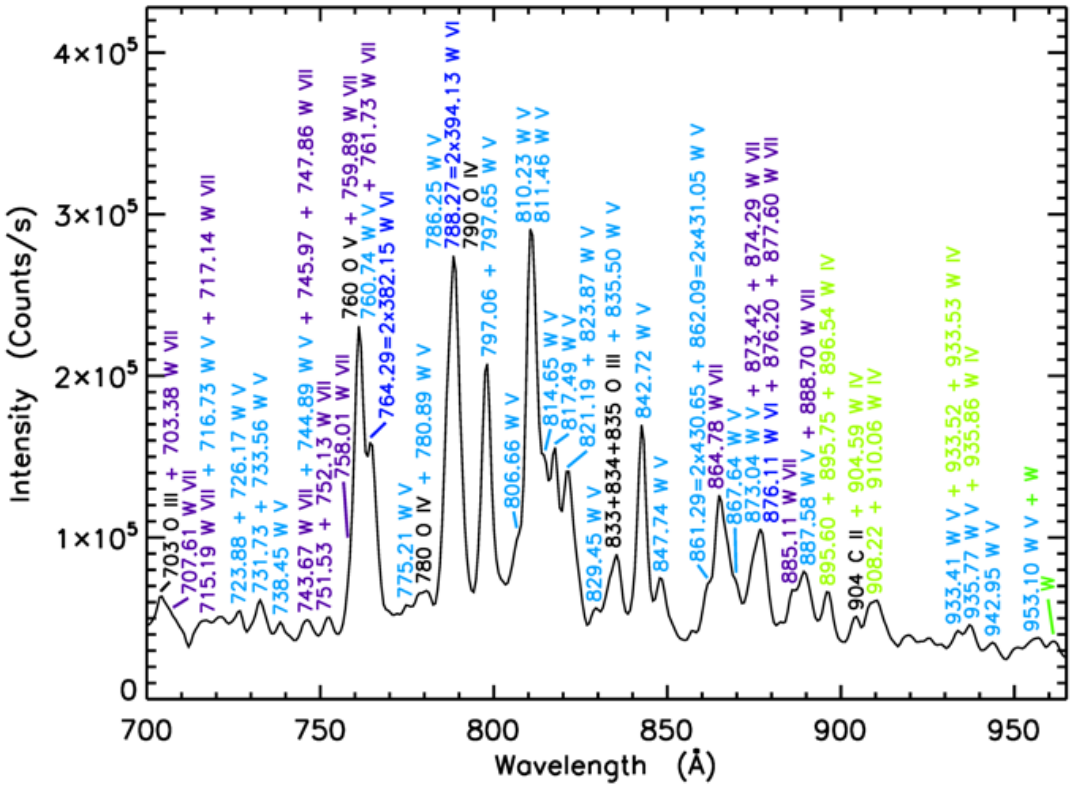

Figure 10. Spectrum of pulse 95012 during a large influx at 54.37 s covering a wavelength range of 700 to 965 Å.

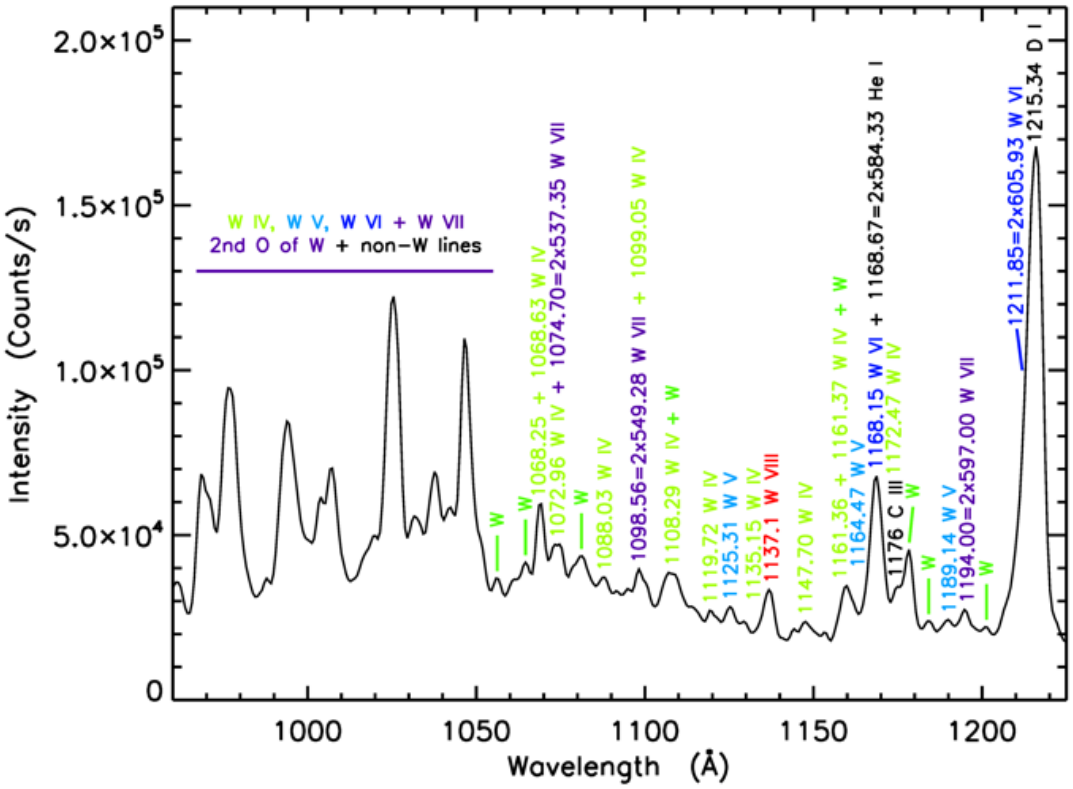

Figure 11a. Spectrum of pulse 95012 during a large influx at 54.37 s covering a wavelength range of 960 to 1225 Å.

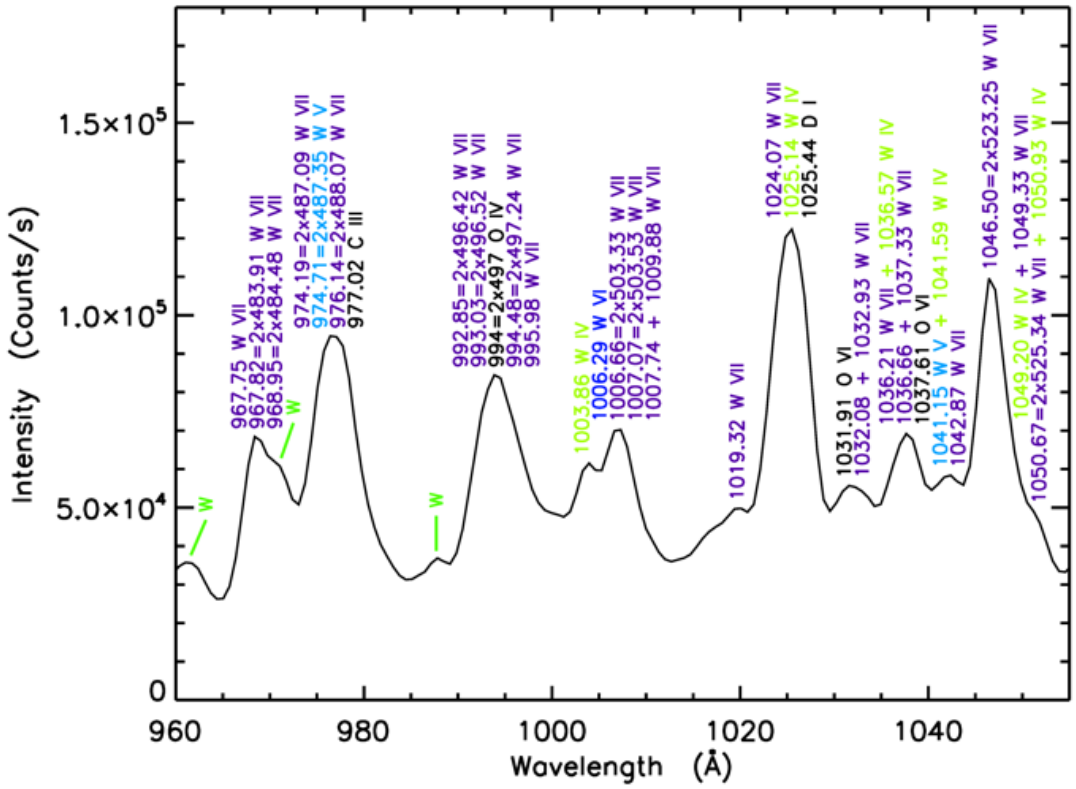

Figure 11b. Spectrum of pulse 95012 during a large influx at 54.37 s covering a wavelength range of 960 to 1017 Å.

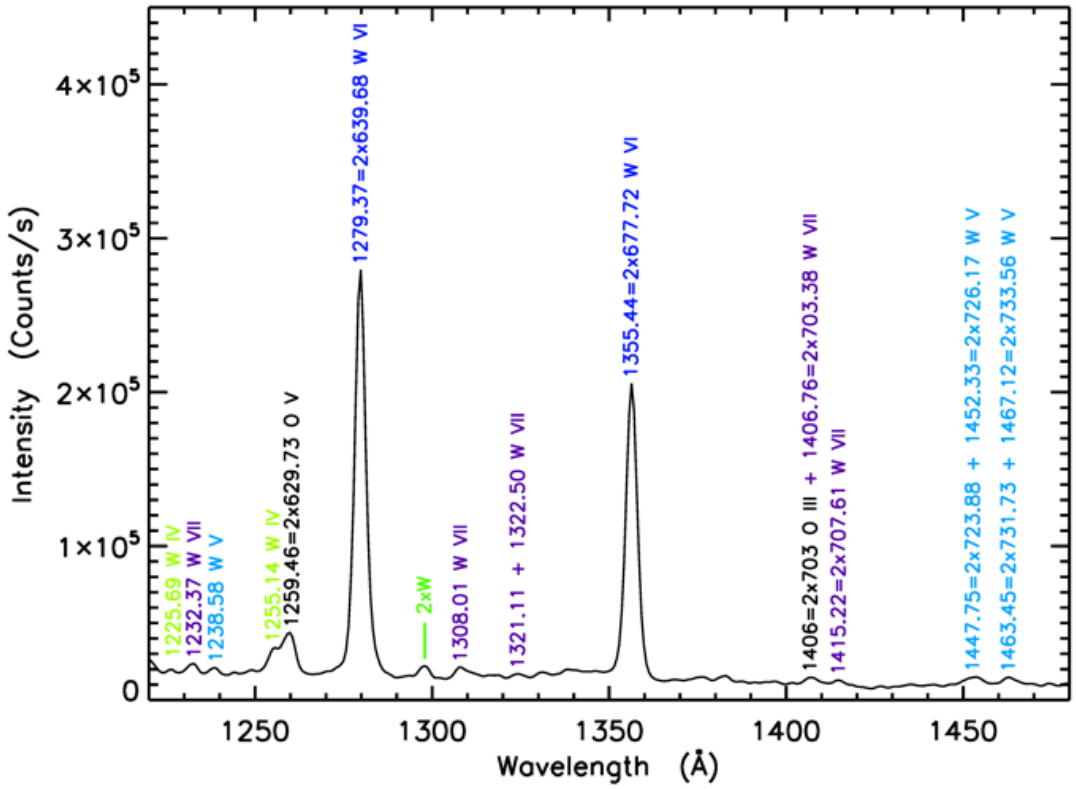

Figure 12. Spectrum of pulse 95012 during a large influx at 54.37 s covering a wavelength range of 1220 to 1480 Å.

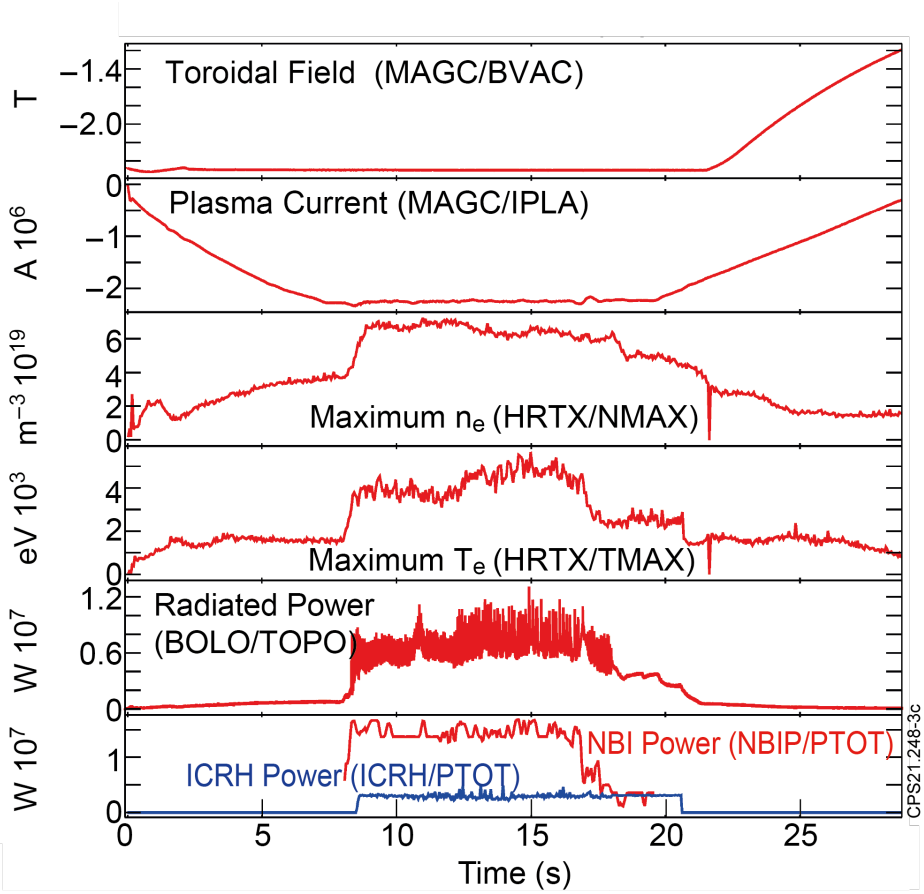

Figure 13. Plasma parameters for pulse 94607.

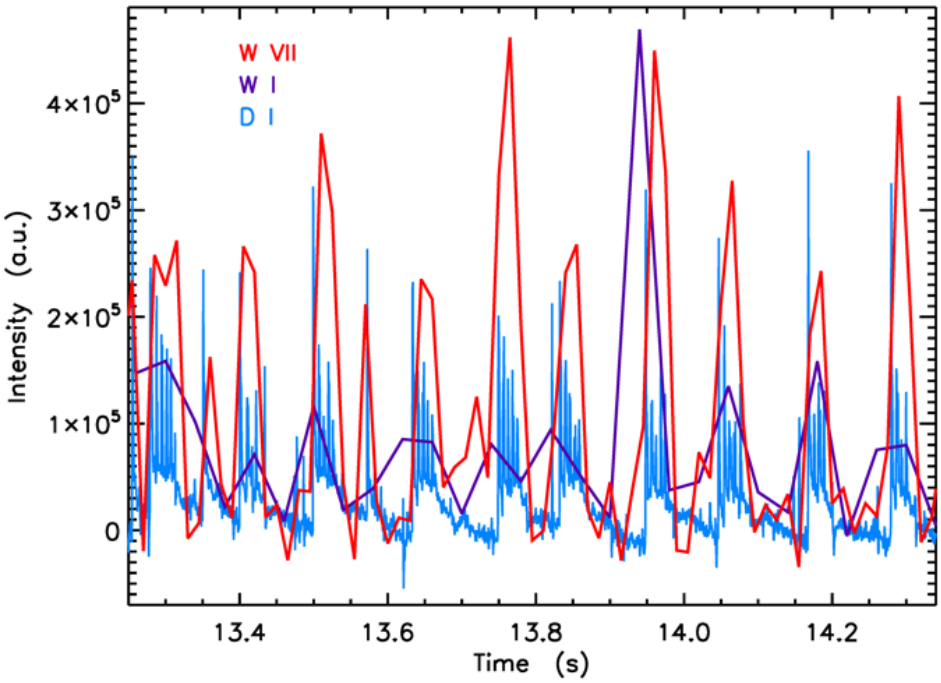

Figure 14. Time histories of 261.39 Å, W VII and 4008.8 Å, W I line intensities in pulse 94607 showing the coincidence with ELMs as indicated by the 6561.0 Å D_α line intensity.

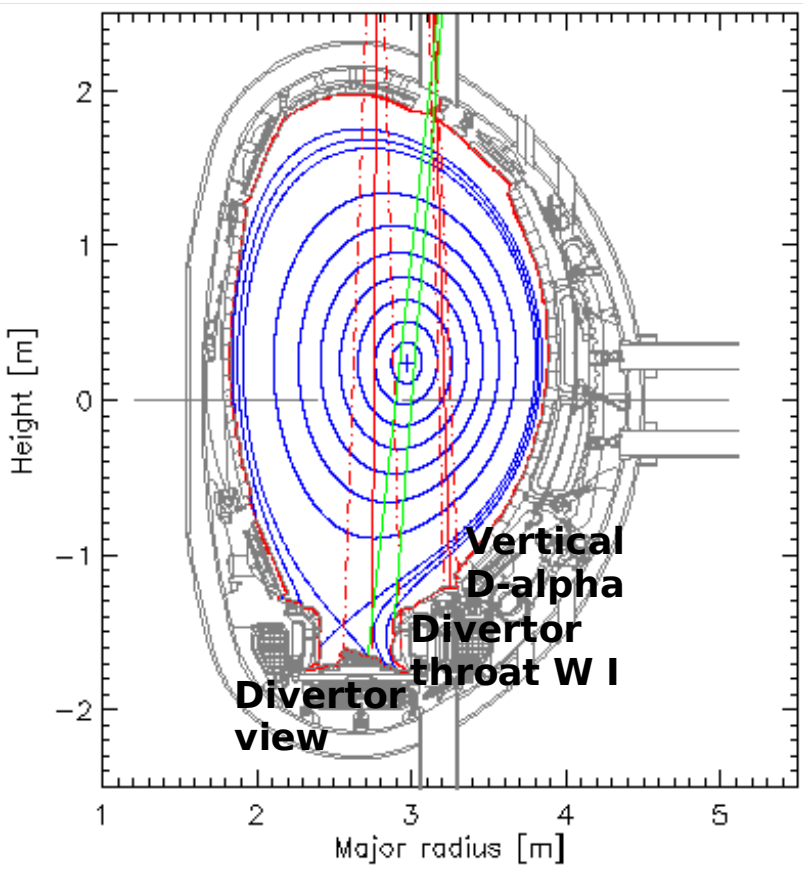

Figure 15. Lines-of-sight of the KS3 (in red) and KT3 (in green) spectrometers, also showing the magnetic configuration at 11 s in pulse 94607.

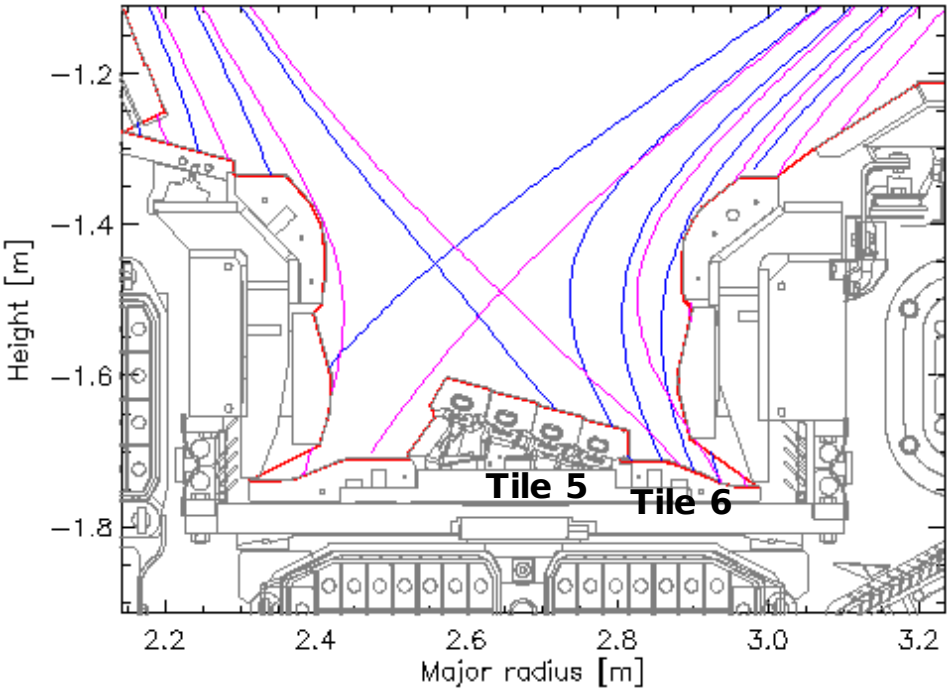

Figure 16. Magnetic configurations of pulse 94607 in the JET divertor at 11 s (outer strike point tile 5 - in blue) and 13 s (tile 6 - in magenta).

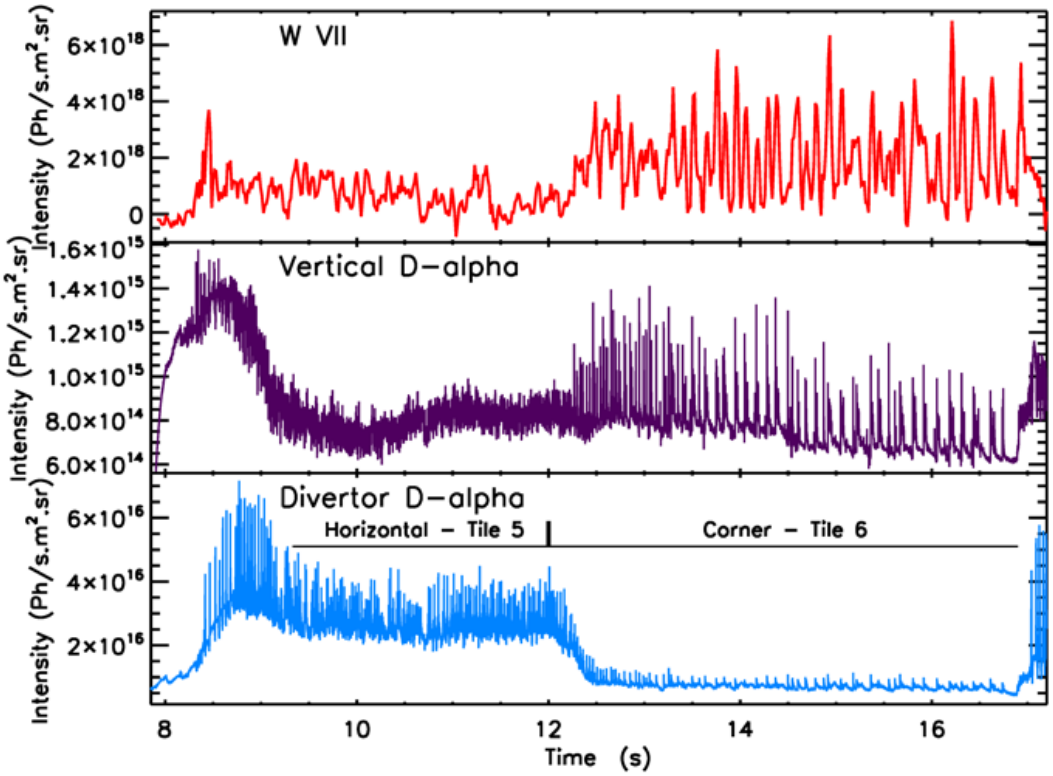

Figure 17. Time histories of 261.39 Å, W VII line intensity together with vertical and divertor D_α in pulse 94607, showing the time periods when the horizontal and corner configurations were used.

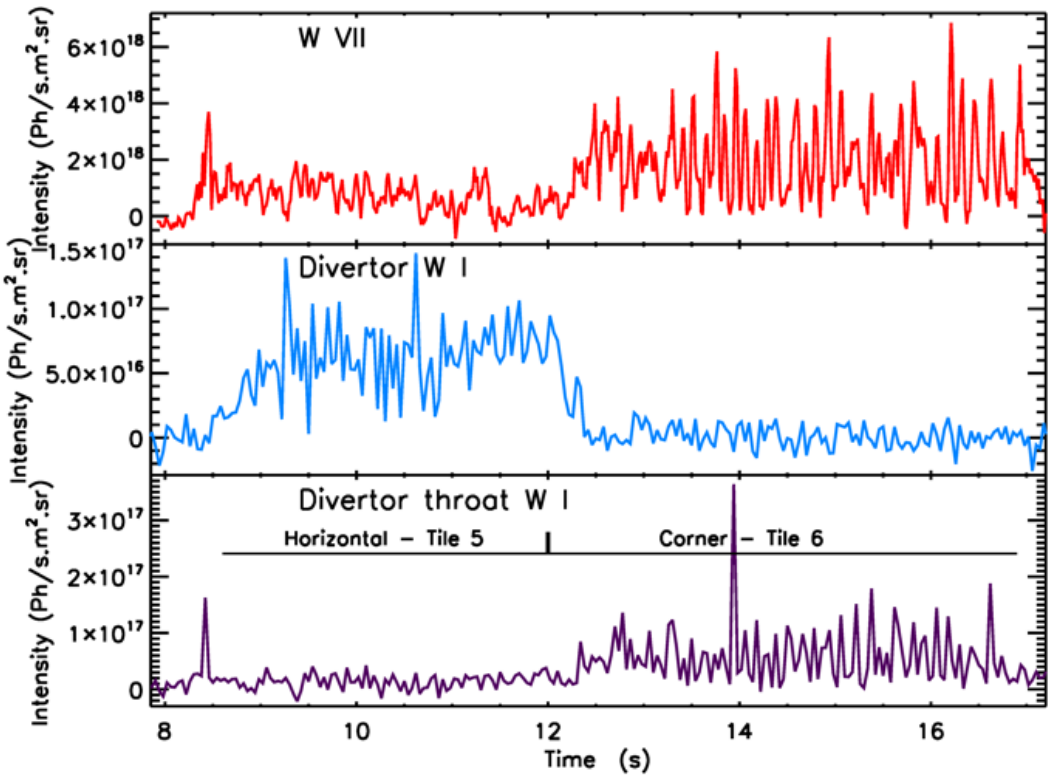

Figure 18. Time histories of 261.39 Å, W VII line intensity together with divertor throat and divertor 4008.8 Å, W I line intensities in pulse 94607, showing the time periods when the horizontal and corner configurations were used.

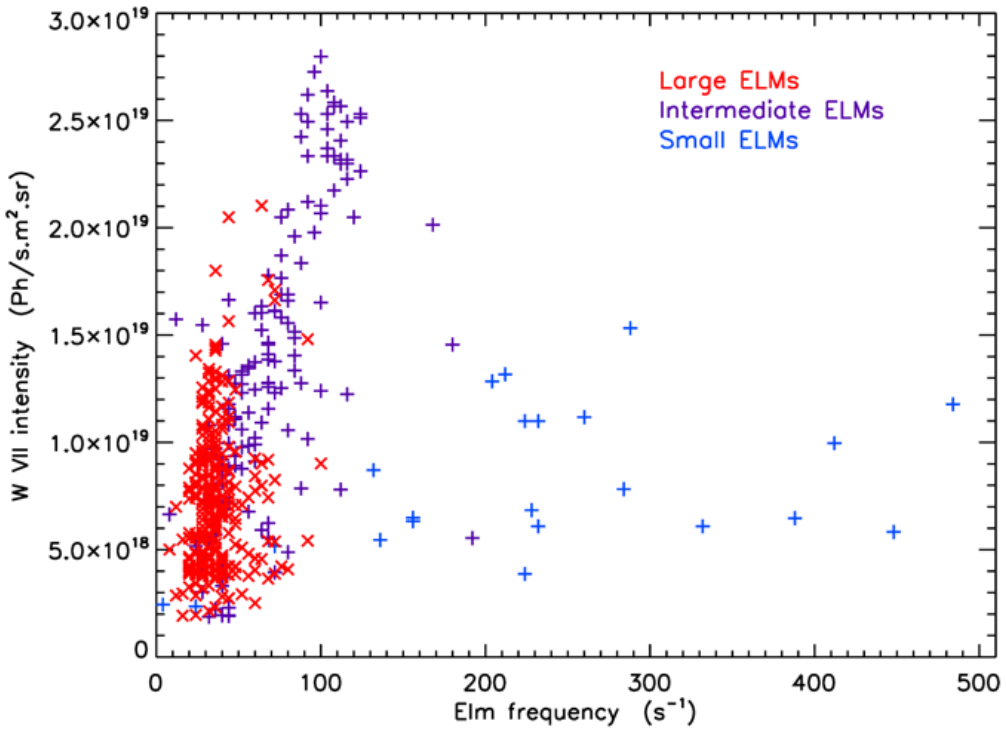

Figure 19. Intensity of the 261.39 Å, W VII line averaged over 0.25 s intervals against ELM frequency. Large ELMs are those with an averaged vertical D-alpha signal > 4×10^{14} ph/s.cm^2.sr, intermediate ELMs between 1 and 4×10^{14} ph/s.cm^2.sr and small ELMs < 1×10^{14} ph/s.cm^2.sr.

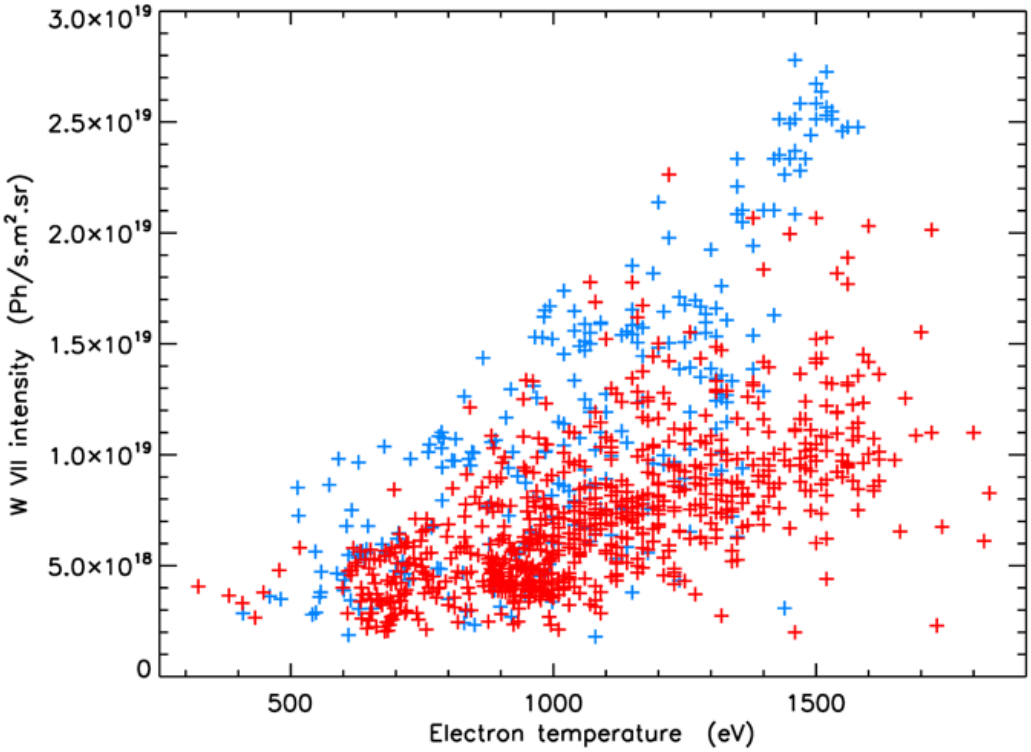

Figure 20. Intensity of 261.39 Å, W VII line averaged over 0.25 s intervals against electron temperature measured using high resolution Thomson scattering at a major radius of 3.7 m. Plasma-wall distance (measured from wall point R=3.33 m, z=-1.07 m) less than 15 mm (in blue); plasma-wall distance greater than 15 mm (in red).

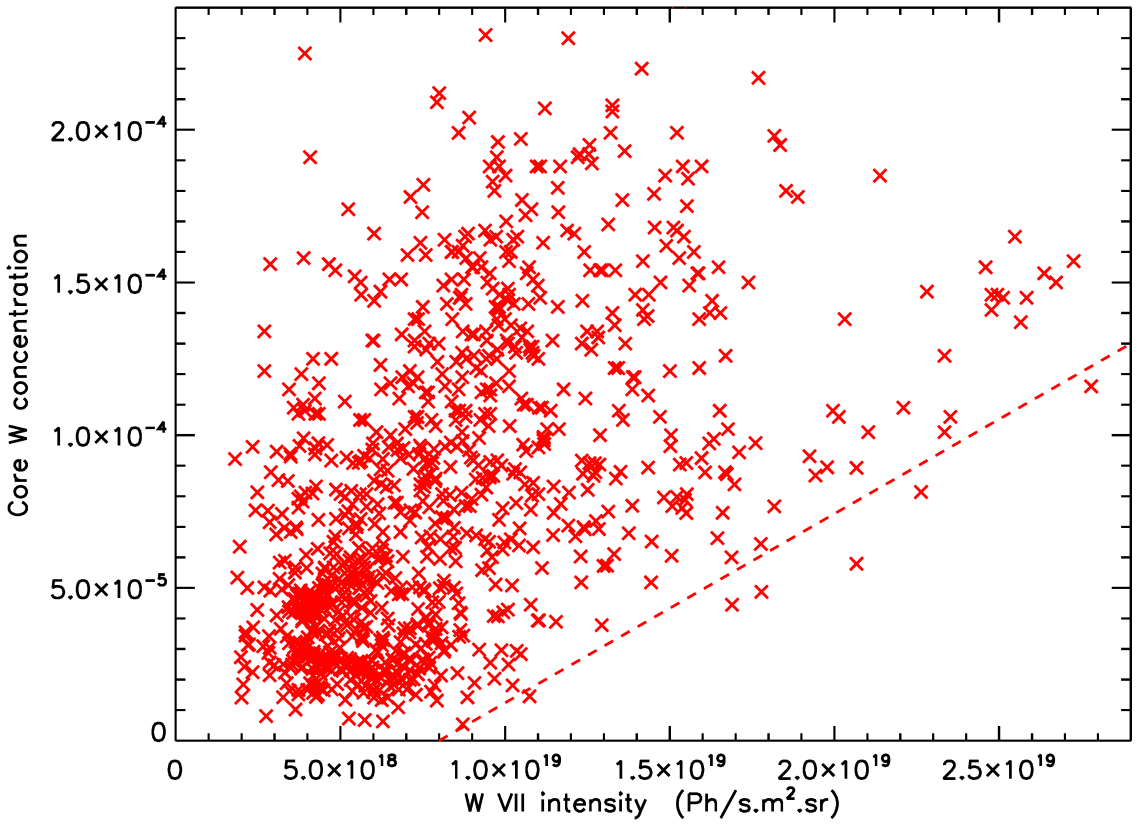

Figure 21. Core W concentration against 261.39 Å, W VII line intensity averaged over intervals of 0.25 s.

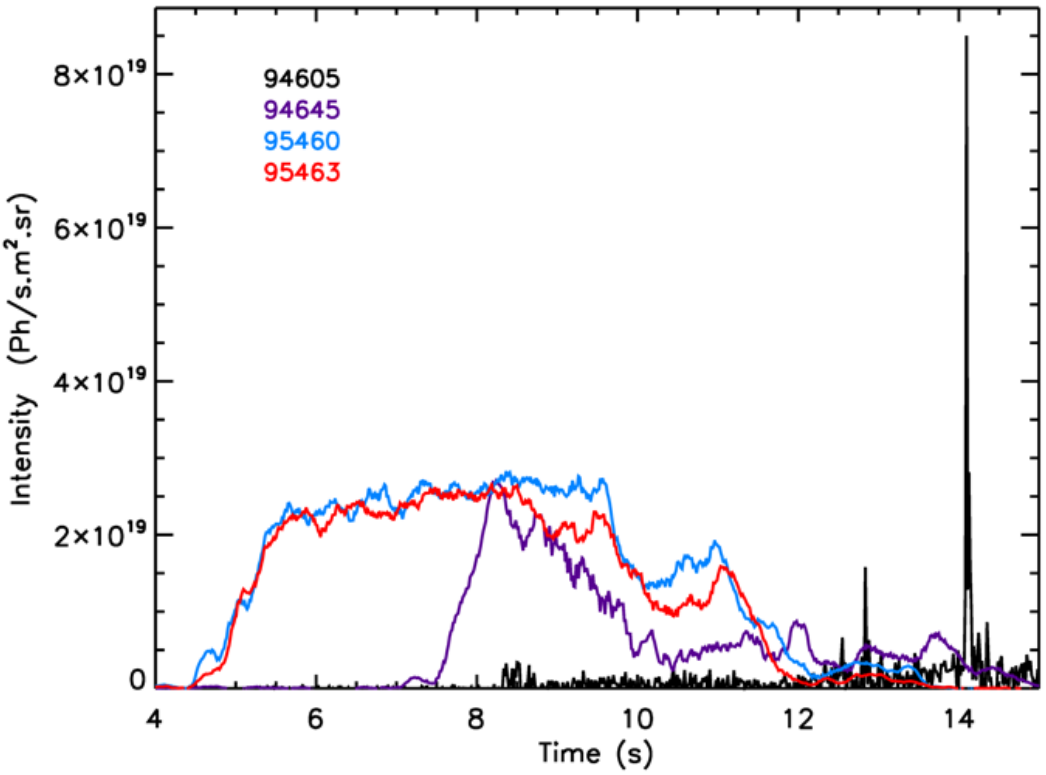

Figure 22. Time histories of intensity of the 261.39 Å, W VII line in pulses 94605, 94645, 95460 and 95463.

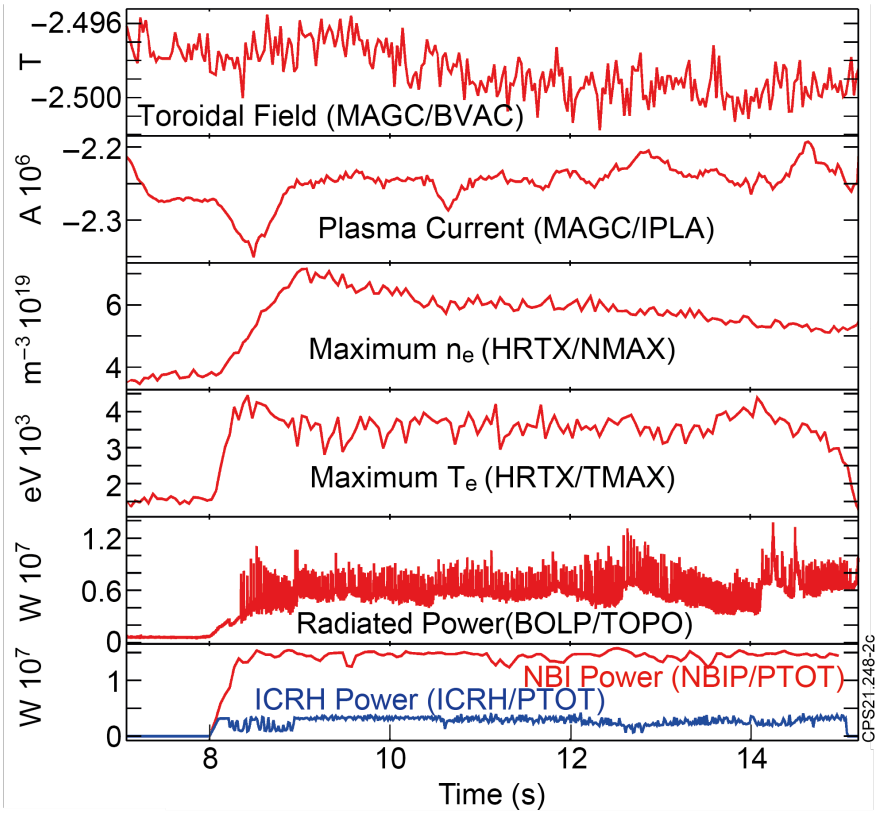

Figure 23. Plasma parameters for pulse 94605.

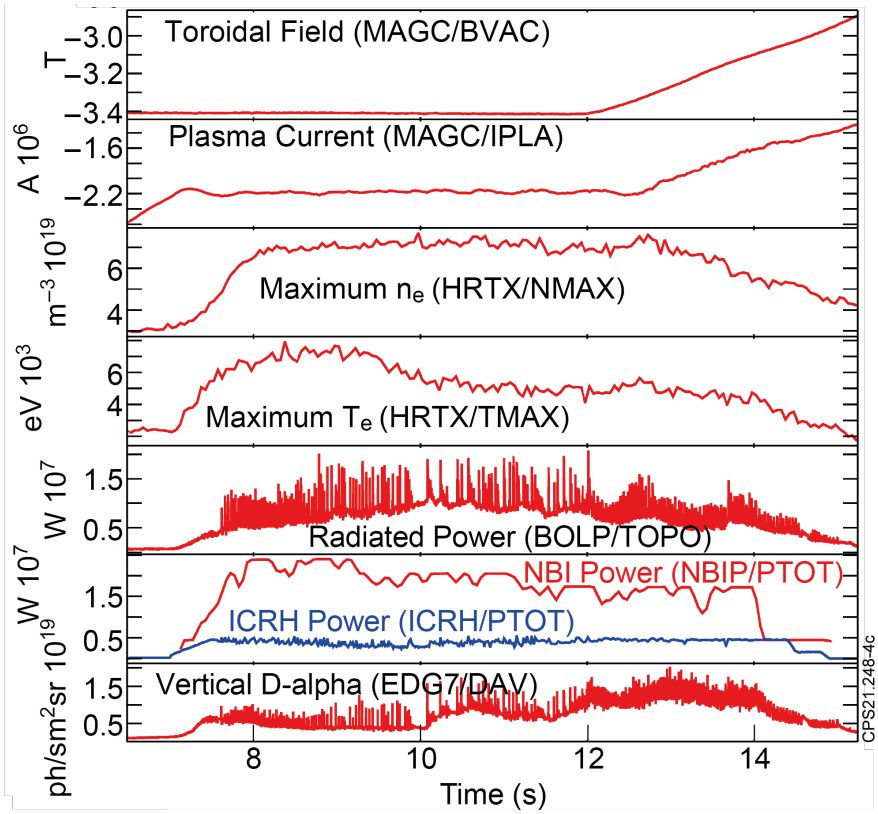

Figure 24. Plasma parameters for pulse 94645.

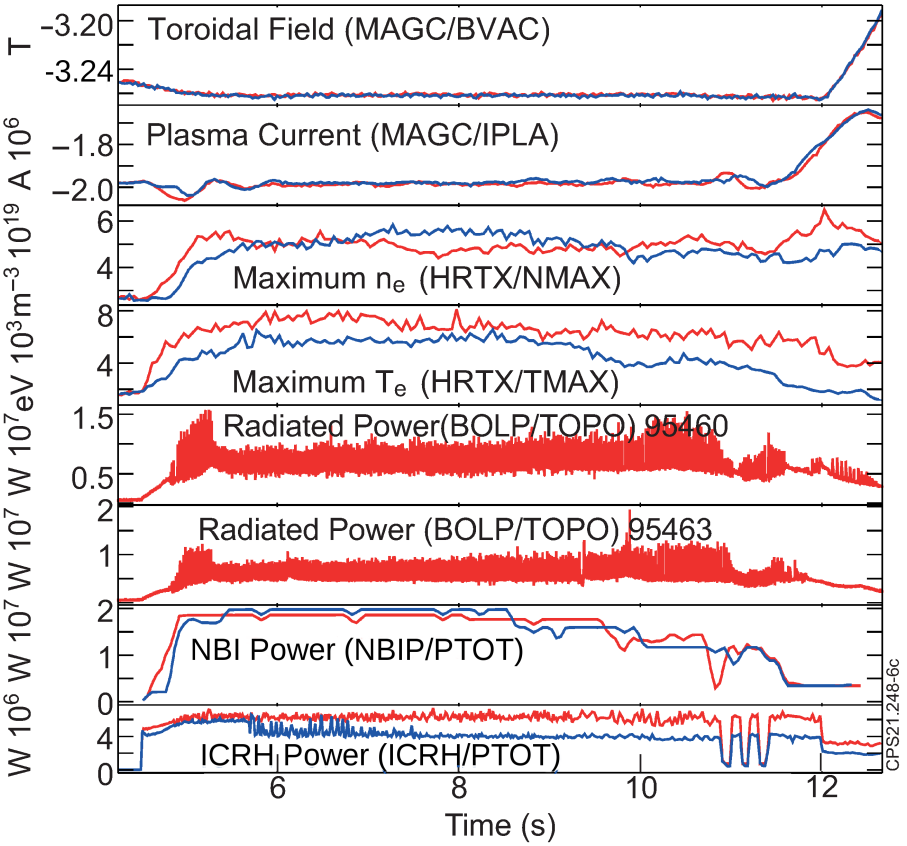

Figure 25. Plasma parameters for pulses 95460 (in red) and 95463 (except for radiated power in blue).

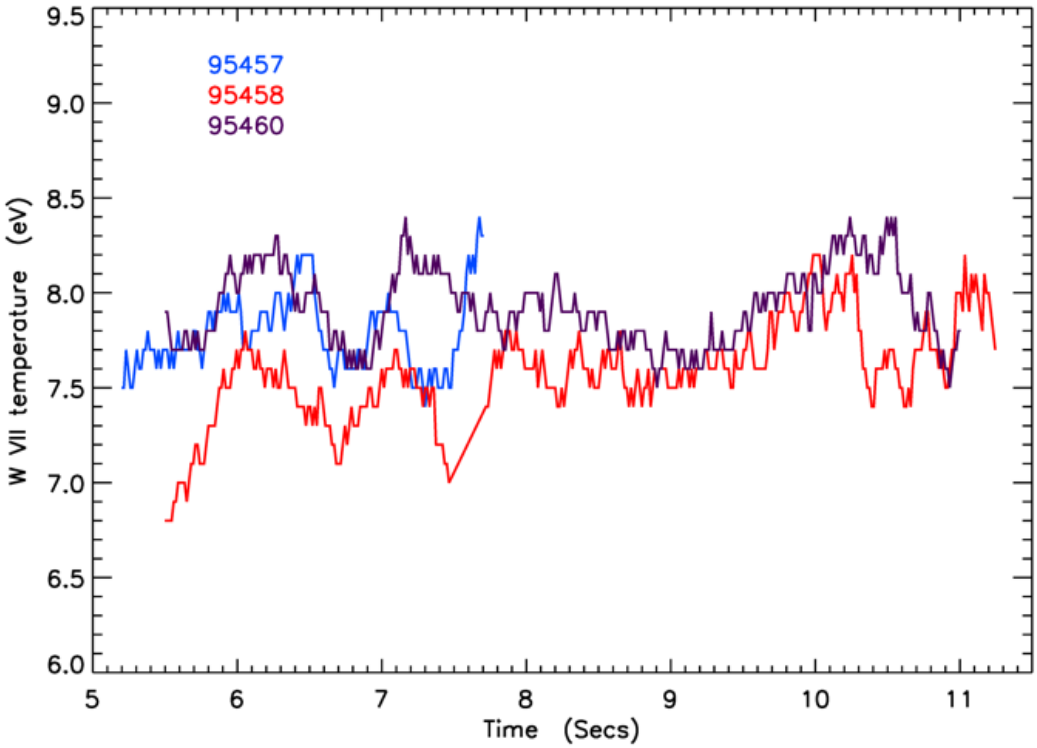

Figure 26. Time histories of electron temperature calculated from W VII line intensity ratios for pulses 95457, 95458 and 95460.

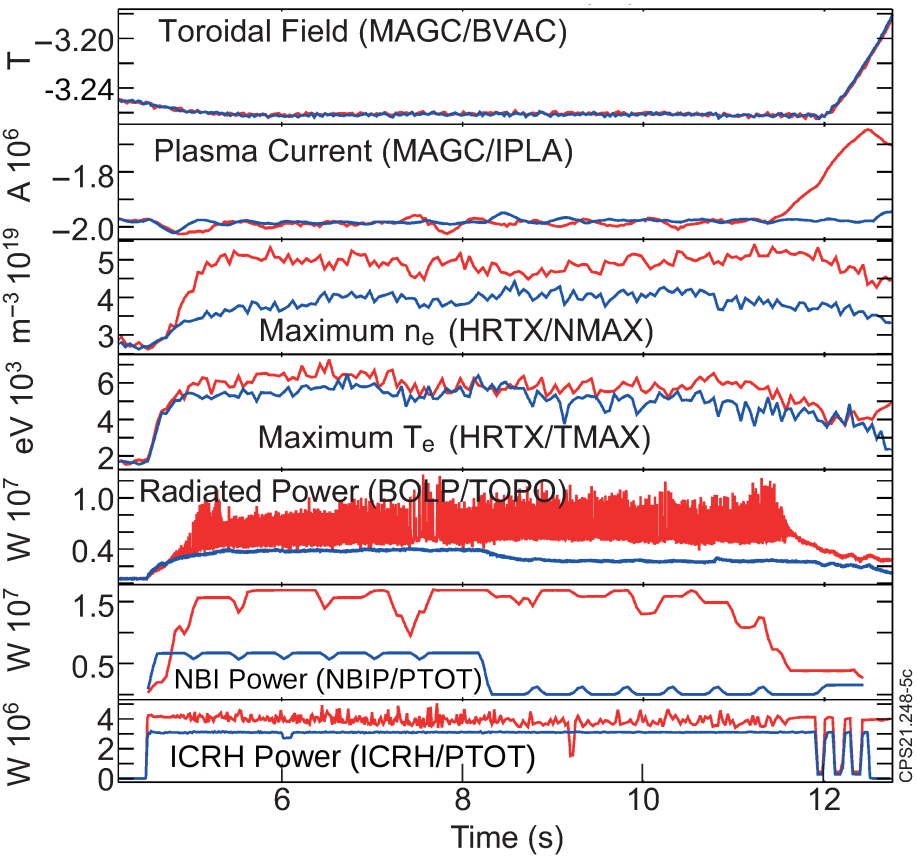

Figure 27. Plasma parameters for pulses 95457 (in blue) and 95458 (in red).